



LJMU Research Online

Battersby, C, Walker, DL, Barnes, A, Ginsburg, A, Lipman, D, Alboslani, D, Hatchfield, HP, Bally, J, Glover, SCO, Henshaw, JD, Immer, K, Klessen, RS, Longmore, SN, Mills, EAC, Molinari, S, Smith, R, Sormani, MC, Tress, RG and Zhang, Q

3D CMZ. II. Hierarchical Structure Analysis of the Central Molecular Zone

<https://researchonline.ljmu.ac.uk/id/eprint/26365/>

Article

Citation (please note it is advisable to refer to the publisher's version if you intend to cite from this work)

Battersby, C, Walker, DL, Barnes, A, Ginsburg, A, Lipman, D, Alboslani, D, Hatchfield, HP, Bally, J, Glover, SCO, Henshaw, JD, Immer, K, Klessen, RS, Longmore, SN, Mills, EAC, Molinari, S, Smith, R, Sormani, MC, Tress, RG and Zhand. O (2025) 3D CMZ. II. Hierarchical Structure Analysis of the

LJMU has developed [LJMU Research Online](#) for users to access the research output of the University more effectively. Copyright © and Moral Rights for the papers on this site are retained by the individual authors and/or other copyright owners. Users may download and/or print one copy of any article(s) in LJMU Research Online to facilitate their private study or for non-commercial research. You may not engage in further distribution of the material or use it for any profit-making activities or any commercial gain.

The version presented here may differ from the published version or from the version of the record. Please see the repository URL above for details on accessing the published version and note that access may require a subscription.

For more information please contact researchonline@ljmu.ac.uk

<http://researchonline.ljmu.ac.uk/>



3D CMZ. II. Hierarchical Structure Analysis of the Central Molecular Zone

Cara Battersby^{1,2}, Daniel L. Walker^{1,3}, Ashley Barnes⁴, Adam Ginsburg⁵, Dani Lipman¹, Danya Albosani¹, H Perry Hatchfield^{1,6}, John Bally⁷, Simon C. O. Glover⁸, Jonathan D. Henshaw^{9,10}, Katharina Immer⁴, Ralf S. Klessen^{2,8,11,12}, Steven N. Longmore^{9,13}, Elisabeth A. C. Mills¹⁴, Sergio Molinari¹⁵, Rowan Smith^{16,17}, Mattia C. Sormani¹⁸, Robin G. Tress¹⁹, and Qizhou Zhang²

¹ University of Connecticut, Department of Physics, 196A Hillside Road, Unit 3046 Storrs, CT 06269-3046, USA

² Center for Astrophysics | Harvard & Smithsonian, MS-78, 60 Garden Street, Cambridge, MA 02138, USA

³ UK ALMA Regional Centre Node, Jodrell Bank Centre for Astrophysics, Oxford Road, The University of Manchester, Manchester M13 9PL, UK

⁴ European Southern Observatory (ESO), Karl-Schwarzschild-Straße 2, 85748 Garching, Germany

⁵ University of Florida Department of Astronomy, Bryant Space Science Center, Gainesville, FL 32611, USA

⁶ Jet Propulsion Laboratory, California Institute of Technology, 4800 Oak Grove Drive, Pasadena, CA 91109, USA

⁷ CASA, University of Colorado, 389-UCB, Boulder, CO 80309, USA

⁸ Universität Heidelberg, Zentrum für Astronomie, Institut für Theoretische Astrophysik, Albert-Ueberle-Str. 2, 69120 Heidelberg, Germany

⁹ Astrophysics Research Institute, Liverpool John Moores University, 146 Brownlow Hill, Liverpool L3 5RF, UK

¹⁰ Max-Planck-Institut für Astronomie, Königstuhl 17, D-69117 Heidelberg, Germany

¹¹ Universität Heidelberg, Interdisziplinäres Zentrum für Wissenschaftliches Rechnen, Im Neuenheimer Feld 225, 69120 Heidelberg, Germany

¹² Radcliffe Institute for Advanced Studies at Harvard University, 10 Garden Street, Cambridge, MA 02138, USA

¹³ Cosmic Origins Of Life (COOL) Research DAO, Germany

¹⁴ Department of Physics and Astronomy, University of Kansas, 1251 Wescoe Hall Drive, Lawrence, KS 66045, USA

¹⁵ INAF—Istituto di Astrofisica e Planetologia Spaziale, Via Fosso del Cavaliere 100, I-00133 Rome, Italy

¹⁶ Scottish Universities Physics Alliance (SUPA), School of Physics and Astronomy, University of St Andrews, North Haugh, St Andrews KY16 9SS, UK

¹⁷ Jodrell Bank Centre for Astrophysics, Department of Physics and Astronomy, University of Manchester, Oxford Road, Manchester M13 9PL, UK

¹⁸ Università dell’Insubria, via Valleggio 11, 22100 Como, Italy

¹⁹ Institute of Physics, Laboratory for Galaxy Evolution and Spectral Modelling, EPFL, Observatoire de Sauverny, Chemin Pegasi 51, 1290 Versoix, Switzerland

Received 2024 October 18; revised 2024 November 27; accepted 2024 December 2; published 2025 May 8

Abstract

The Central Molecular Zone (CMZ) is the way station at the heart of our Milky Way Galaxy, connecting gas flowing in from Galactic scales with the central nucleus. Key open questions remain about its 3D structure, star formation properties, and role in regulating this gas inflow. In this work, we identify a hierarchy of discrete structures in the CMZ using column density maps from Paper I (C. Battersby et al.) We calculate the physical ($N(\text{H}_2)$, T_{dust} , mass, radius) and kinematic (HNCO, HCN, and HC_3N moments) properties of each structure as well as their bolometric luminosities and star formation rates. We compare these properties with regions in the Milky Way disk and external galaxies. Despite the fact that the CMZ overall is well below the Gao–Solomon dense gas star formation relation (and in modest agreement with the Schmidt–Kennicutt relation), individual structures on the scale of molecular clouds generally follow these star formation relations and agree well with other Milky Way and extragalactic regions. We find that individual CMZ structures require a large external pressure ($P_e/k_B > 10^{7-9} \text{ K cm}^{-3}$) to be considered bound; however, simple estimates suggest that most CMZ molecular-cloud-sized structures are consistent with being in pressure-bounded virial equilibrium. We perform power-law fits to the column density probability distribution functions of the inner 100 pc, SgrB2, and the outer 100 pc of the CMZ as well as several individual molecular cloud structures and find generally steeper power-law slopes ($-9 < \alpha < -2$) compared with the literature ($-6 < \alpha < -1$).

Unified Astronomy Thesaurus concepts: Galactic center (565); Star formation (1569); Molecular clouds (1072)

1. Introduction

The inner few hundred parsecs of the Milky Way, known as the “Central Molecular Zone” (CMZ), contains the largest reservoir of dense molecular gas in the Galaxy (M. Morris & E. Serabyn 1996; J. D. Henshaw et al. 2023). The interstellar medium (ISM) in the CMZ is extreme in many ways compared with that of the Galactic disk and may have more similarities with local starburst systems and high- z ($z \sim 2$) galaxies than with regions in the disk (J. M. D. Kruijssen & S. N. Longmore 2013). For example, gas in the CMZ has higher densities (e.g., R. Güsten & C. Henkel 1983; J. Bally et al. 1987; A. Schmiedeke et al. 2016; D. L. Walker et al. 2016; E. A. C. Mills et al. 2018) and temperatures (e.g.,

E. A. C. Mills & M. R. Morris 2013; A. Ginsburg et al. 2016; N. Krieger et al. 2017) than gas in the Galactic disk and is also more turbulent (e.g., J. Bally et al. 1987; R. Shetty et al. 2012; C. Federrath et al. 2016; J. D. Henshaw et al. 2016a, 2016b; J. Kauffmann et al. 2017a; N. Krieger et al. 2020) with stronger magnetic fields (e.g., R. M. Crutcher et al. 1996; T. Pillai et al. 2015). The CMZ is also subject to a stronger UV background field (e.g., D. C. Lis et al. 2001; J. R. Goicoechea et al. 2004; P. C. Clark et al. 2013), higher cosmic-ray ionization rates (e.g., T. Oka et al. 2005; M. Goto et al. 2013; N. Harada et al. 2015; N. Indriolo et al. 2015; M. Padovani et al. 2020), frequent X-ray flares (R. Terrier et al. 2010; M. Clavel et al. 2013; R. Terrier et al. 2018), as well as unique dynamical stresses (e.g., S. N. Longmore et al. 2013b; M. R. Krumholz et al. 2017; M. C. Sormani et al. 2018; J. M. D. Kruijssen et al. 2019; M. C. Sormani et al. 2020; R. G. Tress et al. 2020). J. M. D. Kruijssen & S. N. Longmore (2013) argued that these locally “extreme” properties share



Original content from this work may be used under the terms of the [Creative Commons Attribution 4.0 licence](https://creativecommons.org/licenses/by/4.0/). Any further distribution of this work must maintain attribution to the author(s) and the title of the work, journal citation and DOI.

many similarities with high-redshift galaxies, making the CMZ ideally suited to understand the physics in these distant galaxies up close at a distance of only 8.2 kpc (Gravity Collaboration et al. 2019, 2021; M. J. Reid et al. 2019).

Gas flows into the CMZ from the Galactic disk along the bar dust lanes with an estimated inflow rate of $0.8 \pm 0.6 M_{\odot} \text{ yr}^{-1}$ (e.g., M. C. Sormani & A. T. Barnes 2019; H. P. Hatchfield et al. 2021). Various measurements indicate that the CMZ’s star formation rate (SFR) has been roughly constant over the last 5 Myr at a value of about $0.07 M_{\odot} \text{ yr}^{-1}$ (A. T. Barnes et al. 2017; J. D. Henshaw et al. 2023; H. P. Hatchfield et al. 2024, and references within). The gas inflow is much greater than the SFR, which highlights the importance of the CMZ’s role in regulating gas inflow to the central nucleus. The CMZ engages in prolific star formation in the SgrB2 molecular cloud (e.g., A. Ginsburg et al. 2018; A. Schwörer et al. 2019; F. Meng et al. 2022), but overall has a lower-than-expected SFR (K. Immer et al. 2012; S. N. Longmore et al. 2012). While the CMZ is roughly consistent with the Schmidt–Kennicutt relation between gas and SFR, it falls about an order of magnitude below the Gao–Solomon dense gas–star formation relation (discussed in detail in J. D. Henshaw et al. 2023 and references within). The 3D structure of this region is key to understanding why this region is “under-performing” in star formation and its role in regulating gas inflow from the Galactic disk to the central nucleus. Without an accurate 3D model, we cannot trace gas flows through the CMZ onto the central nucleus, nor can we understand the patterns and causes of its star formation.

Many works have studied the CMZ overall (e.g., A. Ginsburg et al. 2016; J. Kauffmann et al. 2017a, 2017b; N. Krieger et al. 2017; H. P. Hatchfield et al. 2020; X. Lu et al. 2021) or individual regions within (e.g., S. Kendrew et al. 2013; X. Lu et al. 2017; D. L. Walker et al. 2018, 2021). In this work, our aim is to create a comprehensive, hierarchical catalog of structures in the CMZ from the entire CMZ to individual molecular clouds. We apply simple and common analyses that allow us to inter-compare this unique environment with many regions in the literature, from the disk of the Milky Way to more distant galaxies.

This paper is the second in a series focused on understanding the 3D structure of our CMZ. C. Battersby et al. (2025, hereafter Paper I) presents the column density and temperature measurements (derived from modified blackbody fits to Herschel data) that provide the basis of our hierarchical structure catalog. D. L. Walker et al. (2025, hereafter Paper III) performs a comprehensive kinematic analysis of molecular clouds in the catalog and uses molecular line absorption to provide evidence for whether clouds are on the near or far side of the CMZ. D. Lipman et al. (2025, hereafter Paper IV) uses Spitzer $8 \mu\text{m}$ and Herschel $70 \mu\text{m}$ dust extinction maps to constrain the 3D position of clouds in the CMZ and compare with existing models.

This paper is organized as follows. In Section 2 we describe the data used in this work, and the segmentation of the column density map into a hierarchical structure catalog. Section 3 presents the physical and kinematic properties of each structure in this catalog as well as their luminosities and SFRs. This section also presents the method to fit power laws to the column density probability distribution functions (N-PDFs) of select structures in the catalog. The properties derived (sizes, line widths, surface densities, and SFRs) are compared with other Milky Way and extragalactic regions in Section 4. In Section 4 we also plot our power-law slopes against our measured SFRs. We summarize this work and conclude in Section 5.

2. Methods

2.1. Data

In Paper I, we present column density and dust temperature maps of the inner 40° of the Galaxy. These maps were derived by performing modified blackbody fits to Herschel data from $160\text{--}500 \mu\text{m}$ from the Hi-Gal survey (S. Molinari et al. 2011). We smoothed the data to the lowest common resolution of $36''$ (S. Molinari et al. 2016) or about 1.4 pc at the Galactic Center. Using an automated iterative approach, we identified and subtracted the contribution to the Herschel maps from diffuse cirrus emission in the fore/background of the dense structure in our maps. The maps used in this work have been fore/background subtracted and are our best estimate of the dense gas column density and dust temperature in the CMZ on 1 pc scales.

In addition to the Herschel data from Paper I, we take advantage of additional extant data for our analysis. This includes mid-infrared data from the Spitzer space telescope, taken as part of the GLIMPSE (R. A. Benjamin et al. 2003) and MIPS GAL (S. J. Carey et al. 2009) surveys. These data are combined with the Herschel data in a companion paper (A. T. Barnes et al. 2017) to produce bolometric luminosities. We use these luminosities to derive SFRs reported in Table 3 as described in Section 3.5.

We also utilize data from the Mopra 22 m radio telescope of the Australia Telescope National Facility survey of the CMZ, the full observational and data reduction details of which were published by P. A. Jones et al. (2012). In short, Mopra achieved a $39''$ (1.5 pc at the Galactic Center) beam centered on frequencies from $85.3\text{--}93.3 \text{ GHz}$ with an 8 GHz bandpass and $\sim 3.6 \text{ km s}^{-1}$ spectral resolution, sampled in 1.8 km s^{-1} channels. A full kinematic decomposition of the CMZ using the HNC O $4(0,4) - 3(0,3)$ spectral line data is available in J. D. Henshaw et al. (2016b). We use these data to derive approximate kinematic properties of our catalog structures, reported in Table 2 and described in Section 3.3.

2.2. Categorizing the Hierarchical Structure with Dendrograms

A dendrogram is a tree-like diagram that can be used to represent the hierarchical structure of a given data set by segmenting the structure using nested iso-density contours. This technique is used to divide the hierarchical structure in a map into discrete iso-density contours of contiguous and significant emission, and retains information on each structure from largest to smallest scales relevant for a given data set. The use of dendrograms in astronomy is explained in more detail in E. W. Rosolowsky et al. (2008), A. A. Goodman et al. (2009), or R. Shetty et al. (2012), for example. The lowest-level emission forms the “trunk” of the tree, followed by the “branches” and “leaves.” Dendrograms are particularly well suited for regions of complex, hierarchical emission with structures spanning over an order of magnitude in spatial scale. For this reason, we have selected this method to identify structures in the CMZ using our 2D map of column density from Herschel, which is sensitive from scales of 1–100 pc.

We use the python package ASTRODENDRO²⁰ to segment our column density map into a hierarchical structure tree. The dendrogram structure tree and overall map of identified structures is shown in Figure 1. Based on the known structures commonly referred to as clouds in the CMZ and through a

²⁰ <https://dendrograms.readthedocs.io/en/stable/>

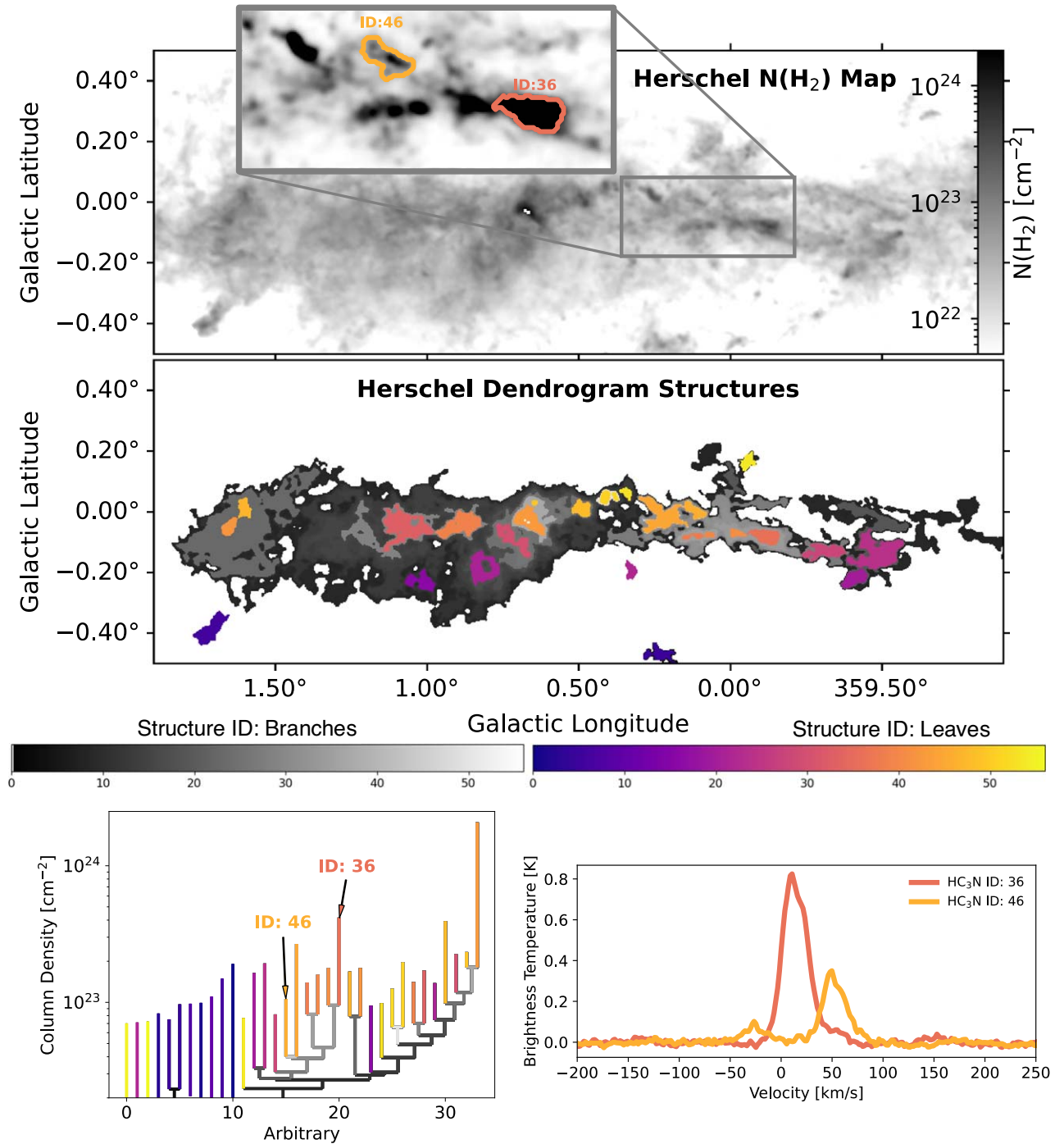


Figure 1. A dendrogram segmentation algorithm is used to create a hierarchical structure catalog from our Herschel column density map (top panel), segmenting the CMZ into its largest scales (structure ID: 9 is the entire CMZ) with a complete hierarchy to individual cloud scales. The middle shows the dendrogram segmentation as a map of structures colored by their IDs, with branches colored in a grayscale color bar and leaves in a plasma color bar. The lower-left panel shows the associated dendrogram tree with the same structure ID color scheme. The zoom-in at the very top highlights two individual clouds in the Herschel column density map, labeled as structures 46 and 36 (the “dust ridge bridge” and 20 km s⁻¹ cloud, respectively). The location of each of these is highlighted in the dendrogram tree on the bottom left, and the associated integrated spectra for these structures in the HC₃N line are shown in the bottom-right panel.

detailed parameter study, we select dendrogram parameters of [MIN_VALUE = 2×10^{22} cm⁻², MIN_DELTA = 5×10^{22} cm⁻², MIN_NPIX = 10] for the decomposition. The minimum value chosen is about a factor of 2 larger than the typical background value in the CMZ of $N(\text{H}_2) = 10^{22}$ cm⁻², while the step size is five times this. While the choice of parameters affects the size of individual regions, and therefore their physical properties, the full range of properties is robustly captured in the structure tree, regardless of the fine-tuning of these parameters. For the

purpose of this and following works in this series, we tuned the dendrogram parameters to optimally capture well-known and long-studied CMZ cloud complexes.

Using the dendrogram parameters described above, we find 11 levels of hierarchical structure in the CMZ, with the highest column density leaf in SgrB. Main. In total, there are 57 structures (branches and leaves) identified. The dendrogram we derive is shown in Figure 1, and the properties of each structure are given in Table 1. The $[\ell, b]$ diagram in Figure 1 shows the

Table 1
General Properties of the Dendrogram Structures

Name	ID	Paper III ID	CMZoom Region	Area (pc ²)	l (°)	b (°)	Median $N(\text{H}_2)$ (cm ⁻²)	Peak $N(\text{H}_2)$ (cm ⁻²)	Mass M (M_\odot)	Radius R (pc)	Density n (cm ⁻³)	Median T_d (K)	Peak T_d (K)	Colloquial Name /Description
Branches														
G0.720-0.069	8	1.3E+04	0.720	-0.069	3.5E+22	2.1E+24	1.5E+07	6.5E+01	1.9E+02	20	36	... ^a
G0.750-0.070	9	1.1E+04	0.750	-0.070	3.9E+22	2.1E+24	1.3E+07	5.9E+01	2.2E+02	20	36	Entire CMZ
G0.970-0.067	11	7.0E+03	0.970	-0.067	4.6E+22	2.1E+24	1.0E+07	4.7E+01	3.3E+02	19	29	Outer 100 pc + SgrB2 + dust ridge
G0.840-0.065	12	5.0E+03	0.840	-0.065	5.2E+22	2.1E+24	7.7E+06	4.0E+01	4.2E+02	20	29	... ^b
G0.830-0.062	13	4.6E+03	0.830	-0.062	5.4E+22	2.1E+24	7.5E+06	3.8E+01	4.7E+02	20	29	... ^b
G0.820-0.059	14	3.6E+03	0.820	-0.059	6.3E+22	2.1E+24	6.6E+06	3.4E+01	5.8E+02	20	27	... ^b
G0.800-0.060	15	2.6E+03	0.800	-0.060	7.4E+22	2.1E+24	5.7E+06	2.9E+01	8.1E+02	20	27	1.1° complex + SgrB2
G359.900-0.071	19	2.0E+03	-0.100	-0.071	4.0E+22	4.2E+23	2.4E+06	2.5E+01	5.3E+02	25	36	Inner 100 pc–dust ridge
G0.020-0.058	27	8, 20	...	1.4E+03	0.020	-0.058	4.1E+22	4.2E+23	1.7E+06	2.1E+01	6.3E+02	25	36	... ^c
G1.610-0.059	23	1.3E+03	1.610	-0.059	4.1E+22	1.8E+23	1.5E+06	2.1E+01	5.6E+02	17	20	1.6° complex
G0.670-0.059	17	1.3E+03	0.670	-0.059	9.4E+22	2.1E+24	3.7E+06	2.0E+01	1.6E+03	21	27	Sgr B2 region
G0.040-0.054	31	12	...	9.4E+02	0.040	-0.054	4.8E+22	4.2E+23	1.4E+06	1.7E+01	9.8E+02	25	36	... ^c
G0.650-0.040	25	8.2E+02	0.650	-0.040	1.1E+23	2.1E+24	3.0E+06	1.6E+01	2.5E+03	21	27	... ^d
G1.040-0.051	29	7.0E+02	1.040	-0.051	7.4E+22	1.7E+23	1.3E+06	1.5E+01	1.3E+03	18	23	1.1° complex
G359.530-0.120	18	1, 3, 5	...	5.4E+02	-0.470	-0.120	4.1E+22	1.9E+23	5.6E+05	1.3E+01	8.8E+02	24	29	SgrC + far-side candidates
G0.670-0.038	26	4.8E+02	0.670	-0.038	1.4E+23	2.1E+24	2.3E+06	1.2E+01	4.6E+03	21	26	...
G359.960-0.078	32	11	...	4.4E+02	-0.040	-0.078	6.4E+22	4.2E+23	8.4E+05	1.2E+01	1.7E+03	24	35	...
G0.660-0.023	37	2.2E+02	0.660	-0.023	1.8E+23	2.1E+24	1.5E+06	8.4E+00	8.7E+03	21	25	...
G0.210-0.003	44	2.2E+02	0.210	-0.003	5.2E+22	2.7E+23	3.3E+05	8.4E+00	1.9E+03	25	28	Dust Ridge Bridge + Brick plus
G359.910-0.079	34	2.2E+02	-0.090	-0.079	9.0E+22	4.2E+23	5.5E+05	8.4E+00	3.2E+03	24	34	50 and 20 km s ⁻¹ Clouds
G0.220-0.490	3	1.2E+02	0.220	-0.490	2.7E+22	9.7E+22	8.4E+04	6.1E+00	1.3E+03	16	25	...
G0.110-0.079	35	8.8E+01	0.110	-0.079	7.3E+22	1.6E+23	1.5E+05	5.3E+00	3.5E+03	23	25	Three Little Pigs
G0.400+0.048	50	5.4E+01	0.400	0.048	7.6E+22	2.0E+23	1.0E+05	4.1E+00	5.0E+03	21	25	Clouds d and c
Leaves														
G359.510-0.130	24	2	34, 36 ^c	2.4E+02	-0.490	-0.130	4.9E+22	1.9E+23	2.9E+05	8.7E+00	1.5E+03	24	28	SgrC
G1.070-0.049	33	29	5, 6	2.2E+02	1.070	-0.049	8.5E+22	1.7E+23	4.6E+05	8.4E+00	2.7E+03	18	23	1.1° Cloud East
G0.230-0.004	45	17	18, 19 [†]	1.6E+02	0.230	-0.004	5.4E+22	2.7E+23	2.5E+05	7.2E+00	2.3E+03	25	28	Brick plus
G0.890-0.044	39	28	7	1.5E+02	0.890	-0.044	9.1E+22	1.4E+23	3.1E+05	6.9E+00	3.3E+03	19	20	1.1° Cloud West
G0.820-0.190	21	27	...	1.3E+02	0.820	-0.190	9.0E+22	1.4E+23	2.6E+05	6.4E+00	3.4E+03	19	20	M0.8-0.2 ring (M. Nonhebel et al. 2024)
G1.720-0.390	6	1.2E+02	1.720	-0.390	3.8E+22	1.5E+23	1.2E+05	6.1E+00	1.8E+03	15	17	...
G0.670-0.028	43	25	9	1.0E+02	0.670	-0.028	3.6E+23	2.1E+24	1.2E+06	5.8E+00	2.1E+04	20	25	Sgr B. Main
G0.720-0.090	30	26	8	1.0E+02	0.720	-0.090	1.4E+23	2.3E+23	3.2E+05	5.7E+00	6.0E+03	20	22	SgrB2 “extended”
G359.690-0.130	28	6	31 [†]	9.8E+01	-0.310	-0.130	3.7E+22	8.2E+22	8.7E+04	5.6E+00	1.7E+03	24	26	bridge from 20 km s ⁻¹ to SgrC
G359.880-0.081	36	9	28	7.8E+01	-0.120	-0.081	1.6E+23	4.2E+23	3.1E+05	5.0E+00	8.6E+03	21	26	20 km s ⁻¹ Cloud
G1.020-0.230	16	7.6E+01	1.020	-0.230	3.6E+22	9.5E+22	6.5E+04	4.9E+00	1.9E+03	20	21	...
G0.550-0.870	0	7.0E+01	0.550	-0.870	3.3E+22	1.9E+23	7.1E+04	4.7E+00	2.4E+03	19	27	...
G359.600-0.220	20	4	33 [†]	6.6E+01	-0.400	-0.220	4.8E+22	1.6E+23	8.1E+04	4.6E+00	2.9E+03	23	25	peak south of SgrC
G0.240-0.470	5	5.8E+01	0.240	-0.470	3.0E+22	7.5E+22	4.4E+04	4.3E+00	1.9E+03	16	25	...
G0.490+0.008	48	23	11	5.4E+01	0.490	0.008	1.4E+23	3.9E+23	2.0E+05	4.1E+00	1.0E+04	20	22	Clouds e and f
G0.120+0.003	46	15	22 [†]	5.0E+01	0.120	0.003	5.3E+22	1.1E+23	6.2E+04	4.0E+00	3.3E+03	25	28	Dust ridge Bridge
G1.600+0.012	47	30	4	4.4E+01	1.600	0.012	9.7E+22	1.7E+23	1.0E+05	3.7E+00	6.8E+03	16	17	1.6° Cloud North
G1.650-0.052	42	31	3	4.4E+01	1.650	-0.052	1.0E+23	1.8E+23	1.0E+05	3.7E+00	6.8E+03	15	16	1.6° Cloud South
G359.940+0.160	54	3.8E+01	-0.060	0.160	3.2E+22	7.7E+22	3.2E+04	3.5E+00	2.6E+03	19	24	...

Table 1
(Continued)

Name	ID	Paper III ID	CMZoom Region	Area (pc ²)	l (°)	b (°)	Median $N(\text{H}_2)$ (cm ⁻²)	Peak $N(\text{H}_2)$ (cm ⁻²)	Mass M (M_\odot)	Radius R (pc)	Density n (cm ⁻³)	Median T_d (K)	Peak T_d (K)	Colloquial Name /Description
G0.330-0.190	22	18	17	3.4E+01	0.330	-0.190	2.8E+22	7.1E+22	2.5E+04	3.3E+00	2.4E+03	22	27	...
G3.430-0.350	10	3.4E+01	3.430	-0.350	3.4E+22	1.1E+23	2.9E+04	3.3E+00	2.8E+03	15	20	...
G0.200-0.520	4	3.2E+01	0.200	-0.520	3.0E+22	9.7E+22	2.7E+04	3.2E+00	2.8E+03	16	18	...
G0.410+0.048	51	21	12	2.6E+01	0.410	0.048	9.7E+22	2.0E+23	6.2E+04	2.9E+00	8.8E+03	21	23	Cloud d
G359.980-0.071	41	10	26	2.2E+01	-0.020	-0.071	1.2E+23	1.8E+23	6.2E+04	2.6E+00	1.2E+04	24	25	50 km s ⁻¹ Cloud
G0.340+0.060	53	19	15	2.0E+01	0.340	0.060	4.8E+22	9.9E+22	2.5E+04	2.5E+00	5.5E+03	23	26	Cloud b
G0.120-0.081	38	14, 16	20, 21	2.0E+01	0.120	-0.081	9.0E+22	1.4E+23	4.4E+04	2.5E+00	9.7E+03	22	23	Straw and Sticks Clouds
G358.460-0.390	7	1.7E+01	-1.540	-0.390	3.3E+22	9.8E+22	1.5E+04	2.3E+00	4.3E+03	17	18	...
G356.660+0.560	56	1.4E+01	-3.340	0.560	2.6E+22	7.3E+22	9.1E+03	2.1E+00	3.4E+03	11	13	...
G0.070-0.076	40	13	23	1.2E+01	0.070	-0.076	1.1E+23	1.6E+23	3.0E+04	1.9E+00	1.5E+04	21	22	Stone Cloud
G0.090-0.660	2	1.1E+01	0.090	-0.660	3.0E+22	8.3E+22	8.7E+03	1.9E+00	4.4E+03	18	20	...
G0.380+0.050	52	21	14	9.0E+00	0.380	0.050	8.7E+22	1.3E+23	1.8E+04	1.7E+00	1.3E+04	21	24	Cloud c
G356.520+0.210	55	8.0E+00	-3.480	0.210	2.4E+22	7.0E+22	5.2E+03	1.6E+00	4.4E+03	13	13	...
G357.070-0.770	1	7.0E+00	-2.930	-0.770	2.9E+22	9.9E+22	5.0E+03	1.5E+00	5.1E+03	9	12	...
G0.650+0.030	49	24	...	6.0E+00	0.650	0.030	2.0E+23	2.3E+23	2.8E+04	1.4E+00	3.5E+04	19	20	Small isolated peak in SgrB2

Notes. Shown for each structure is the source name, structure ID, corresponding leaf IDs in Paper III, corresponding region ID in the CMZoom survey, exact dendrogram area in parsec², central coordinates in degrees [l , b], median and peak column density ($N(\text{H}_2)$), mass, radius (assuming the radius of a circle of equivalent area), volume density (assuming spherical symmetry), median and peak dust temperature (T_d), and colloquial name in the literature (where applicable). Structures are grouped by type (branch or leaf), and ordered within each group by descending area. The dagger symbol indicates structures that have only small/partial overlap with the noted CMZoom region.

^a Structure 8 is the entire CMZ along with an isolated peak.

^b Structures 12, 13, and 14 are all variations on the 1.1 complex + SgrB2 + dust ridge hierarchy with isolated peaks.

^c Structures 27, 31, and 32 are variations on the Inner 100 pc–dust ridge hierarchy. Structure 31 contains SgrA*, but its contribution to the average physical properties of this large region is negligible at far-IR wavelengths.

^d Structures 25, 26, and 37 are all part of the Sgr B2 hierarchy.

^e Structures 20, 24, 28, and 45 are only partially covered by CMZoom.

spatial extent of each dendrogram structure, colored by the object’s structure ID from 0–56 based on the order in which structures are decomposed by the algorithm and without any physical significance. The corresponding dendrogram tree displayed in the lower-left panel of Figure 1 shows the full hierarchical tree as related to the peak column density of each structure on the y -axis. The “trunk” of the CMZ hierarchy is a single structure (ID: 9)—a single, contiguous emission feature in $[\ell, b]$ space, that is at the base of the large tree. The remaining structures outside this large tree in the lower-left panel of Figure 1 are isolated features in $[\ell, b]$ space, not associated with the rest of the CMZ hierarchy.

3. Analysis

3.1. Table Overview

We report on the physical and kinematic properties of each dendrogram structure derived in this work in Tables 1 and 2

and on their luminosities in Table 3. Table 1 reports on the name, structure ID, physical area, central coordinates, median and peak column density, mass, effective radius, median and peak dust temperature, as well as a colloquial name for each structure or a brief description. Table 2 reports on the moment 0, 1, and 2 results for the HNC0 $4_{0,4} - 3_{0,3}$, HCN $1 - 0$, and HC₃N $10 - 9$ transitions. Table 3 reports on luminosities and SFRs inferred from the Paper I modified blackbody fits.

The catalog presented here is for the full CMZ hierarchy. D. L. Walker et al. (2025, hereafter Paper III) is focused on the individual molecular clouds in the CMZ within this hierarchy. Therefore, in Paper III, we create a molecular cloud catalog using primarily the leaves of the dendrogram structures from this work with a few small changes. Full details are described in Paper III, but the changes include: adding a few lower column density molecular clouds to the catalog that are at critical positions in the CMZ orbit for determining near/far distances, splitting the Straw and Sticks molecular clouds

Table 2
Kinematic Properties of the Dendrogram Structures

Name	ID	Integrated Intensity			Weighted Velocity			FWHM		
		(K km s ⁻¹)			(km s ⁻¹)			(km s ⁻¹)		
		HNC0	HCN	HC ₃ N	HNC0	HCN	HC ₃ N	HNC0	HCN	HC ₃ N
		$4_{0,4} - 3_{0,3}$	$1 - 0$	$10 - 9$	$4_{0,4} - 3_{0,3}$	$1 - 0$	$10 - 9$	$4_{0,4} - 3_{0,3}$	$1 - 0$	$10 - 9$
Branches										
G0.720-0.069	8	1.4E-02	6.3E-02	6.0E-03	57	67	51	72	95	79
G0.750-0.070	9	1.6E-02	6.8E-02	6.6E-03	56	66	50	70	94	76
G0.970-0.067	11	2.1E-02	7.2E-02	7.7E-03	58	72	54	67	88	73
G0.840-0.065	12	2.2E-02	8.1E+01	9.2E+00	59	73	53	73	88	75
G0.830-0.062	13	2.4E-02	8.3E+01	9.7E+00	58	72	53	73	88	74
G0.820-0.059	14	2.9E-02	8.8E+01	1.1E+01	57	71	52	71	87	72
G0.800-0.060	15	3.3E-02	9.2E+01	1.3E+01	55	70	51	68	87	68
G359.900-0.071	19	8.9E-03	7.6E+01	6.9E+00	32	45	36	84	94	74
G0.020-0.058	27	1.2E-02	9.5E+01	9.0E+00	34	48	37	72	83	67
G1.610-0.059	23	1.6E-02	4.4E-02	4.1E-03	51	64	53	26	67	30
G0.670-0.059	17	4.2E-02	1.1E+02	1.8E+01	46	63	46	49	87	52
G0.040-0.054	31	1.5E-02	1.1E+02	1.1E+01	34	47	37	65	77	61
G0.650-0.040	25	4.7E-02	1.1E+02	2.1E+01	49	63	48	48	86	52
G1.040-0.051	29	2.7E-02	8.1E+01	7.5E+00	83	80	81	24	72	32
G359.530-0.120	18	7.2E-03	5.1E+01	4.9E+00	-55	-45	-50	37	150	80
G0.670-0.038	26	5.6E-02	1.2E+02	2.5E+01	53	66	53	43	84	45
G359.960-0.078	32	2.0E-02	1.2E+02	1.6E+01	29	43	34	61	72	58
G0.660-0.023	37	6.5E-02	1.2E+02	3.0E+01	58	73	59	31	80	29
G0.210-0.003	44	1.3E-02	9.9E+01	7.9E+00	46	54	44	64	78	63
G359.910-0.079	34	2.6E-02	1.3E+02	2.1E+01	22	37	28	48	73	56
G0.220-0.490	3
G0.110-0.079	35	2.1E-02	1.4E+02	1.3E+01	53	52	52	25	56	23
G0.400+0.048	50	1.8E-02	6.0E+01	8.6E+00	17	28	16	32	43	38
Leaves										
G359.510-0.130	24	9.7E-03	5.6E+01	5.6E+00	-56	-42	-55	22	130	26
G1.070-0.049	33	2.7E-02	6.9E+01	6.1E+00	84	79	79	21	71	32
G0.230-0.004	45	1.4E-02	9.3E+01	7.1E+00	42	53	35	70	81	65
G0.890-0.044	39	3.5E-02	9.0E+01	9.7E+00	83	77	48	20	68	120
G0.820-0.190	21	4.3E-02	1.0E+02	1.6E+01	39	69	40	34	86	33
G1.720-0.390	6
G0.670-0.028	43	8.1E-02	1.3E+02	4.2E+01	62	76	61	29	76	27
G0.720-0.090	30	6.0E-02	1.3E+02	2.6E+01	39	59	32	54	82	50
G359.690-0.130	28	6.4E-03	4.0E+01	2.4E+00	-26	4	-27	24	140	16
G359.880-0.081	36	3.8E-02	1.2E+02	2.6E+01	15	24	15	27	55	29
G1.020-0.230	16	5.9E-03	4.0E+01	1.5E+00	97	96	92	55	75	54
G0.550-0.870	0
G359.600-0.220	20	5.4E-03	5.8E+01	7.1E+00	-13	-20	-34	95	170	120

Table 2
(Continued)

Name	ID	Integrated Intensity			Weighted Velocity			FWHM		
		(K km s ⁻¹)			(km s ⁻¹)			(km s ⁻¹)		
G0.240-0.470	5
G0.490+0.008	48	3.3E-02	9.0E+01	1.3E+01	28	40	30	25	55	24
G0.120+0.003	46	1.3E-02	1.0E+02	1.2E+01	52	56	54	26	64	28
G1.600+0.012	47	3.1E-02	5.3E+01	5.8E+00	53	89	52	23	150	19
G1.650-0.052	42	2.9E-02	3.9E+01	7.5E+00	50	59	51	15	23	12
G359.940+0.160	54	6.8E-04	1.0E+01	5.3E-01	-110	55	0	100	140	4
G0.330-0.190	22	1.4E-03	1.6E+01	5.7E-01	16	20	18	29	12	5
G3.430-0.350	10
G0.200-0.520	4
G0.410+0.048	51	2.4E-02	6.6E+01	1.0E+01	19	28	18	25	38	28
G359.980-0.071	41	3.3E-02	1.8E+02	3.8E+01	48	53	47	25	58	26
G0.340+0.060	53	7.9E-03	3.8E+01	5.3E+00	-2	19	-3	34	60	38
G0.120-0.081	38	2.6E-02	1.5E+02	1.6E+01	54	54	53	22	54	22
G358.460-0.390	7
G356.660+0.560	56
G0.070-0.076	40	3.0E-02	1.7E+02	2.2E+01	50	51	51	22	50	21
G0.090-0.660	2
G0.380+0.050	52	1.1E-02	5.1E+01	5.5E+00	14	28	11	49	47	52
G356.520+0.210	55
G357.070-0.770	1
G0.650+0.030	49	7.4E-02	1.3E+02	2.7E+01	53	67	52	28	70	30

Note. Shown for each structure is the source name, leaf ID, and moment-analysis-computed integrated intensity (mom0), centroid velocity (mom1), and velocity FWHM, for HNC0 4_{0,4} – 3_{0,3}, HCN 1 – 0, and HC₃N 10 – 9. The grouping and order of structures is the same as in Table 1.

(structure ID 38 in this work) into two clouds for the Paper III analysis, and excluding leaves that are isolated and not part of the CMZ hierarchy. The final molecular cloud catalog is also re-numbered to be ordered with Galactic longitude. The molecular cloud catalog is described in detail in Paper III. We include in Table 1 the relevant Paper III cloud IDs for easy inter-comparison. We also list the approximate region IDs from the CMZoom Survey (C. Battersby et al. 2020; H. P. Hatchfield et al. 2020) for comparison.

The derivation of these physical properties is described in Section 3.2, the kinematic properties in Section 3.3, and the luminosities and SFRs in Section 3.4. All three tables, Tables 1, 2, 3, have identical row organization. The structures are separated by whether they are categorized as branches (listed first) or leaves (listed second). Then, within each category, the structures are listed in order of decreasing total structure area.

We release all of the analysis products from this series of papers (including the dendrogram masks and a full machine-readable table including all columns from Tables 1 to 4) in the 3D CMZ Harvard Dataverse.²¹ The data set for this paper is found in the Papers I and II repository: DOI:10.7910/DVN/7DOJG5 (C. Battersby et al. 2024). The Harvard Dataverse is a data repository that enables long-term data preservation and sharing. Project updates can also be found on the 3D CMZ website.²²

3.2. Physical Properties of CMZ Structures

Most of the calculations of physical properties tabulated in Table 1 are fairly straightforward, but we describe here some of the details and nuances. The source name is from the source

²¹ https://dataverse.harvard.edu/dataverse/3D_CMZ

²² https://centralmolecularzone.github.io/3D_CMZ/

coordinates, which is the dendrogram-specified purely geometric mean position of the overall structure mask in x and y . The structure ID is computed by the dendrogram algorithm and does not have physical meaning. We also include a colloquial name or description of key structures in the final column of Table 1. For detailed exploration of the catalog or comparison with other data, please download the dendrogram mask directly from our Dataverse (see link at the end of Section 3.1).

The area for each structure is simply the number of pixels contained in the dendrogram mask multiplied by the pixel area at a Galactic Center distance of 8.2 kpc (assumed throughout this work). The median and peak column densities for each structure are from the Herschel column density map from Paper I. The mass is the average column density of each structure multiplied by its area. As described in Paper I, this mass is therefore our best estimate of the total molecular gas.

We report a radius for each structure, which is defined as the radius of a circle whose area equals the total dendrogram mask area. The volume density is calculated assuming that this radius (which is derived from a 2D plane-of-sky projection) corresponds to the true average 3D radius of the structure. We divide the total structure mass by the volume of a 3D sphere with this radius. This assumption is reasonable for leaves, but not very realistic for the branches and other large structures in the hierarchy. We report both a median and peak dust temperature within each structure from the dust temperature map in Paper I.

3.3. Kinematic Properties of CMZ Structures

We report simple kinematic properties of each dendrogram structure using 3 mm data from the Mopra radio telescope from P. A. Jones et al. (2012) in Table 2. We report the properties of three spectral lines: HNC0 4(0,4) – 3(0,3) at 87.925238 GHz,

Table 3
Luminosity, SFR, and Confinement Properties of the Dendrogram Structures

Name	ID	L_{tot} (Cool) (L_{\odot})	$\langle L \rangle$ (Cool) ($L_{\odot} \text{ pix}^{-1}$)	L_{tot} (Warm) (L_{\odot})	$\langle L \rangle$ (Warm) ($L_{\odot} \text{ pix}^{-1}$)	L_{totalIR} (L_{\odot})	$\text{SFR}_{\text{totalIR}}$ ($M_{\odot} \text{ yr}^{-1}$)	t_{ff} (Myr)	SFR_{FF} ($M_{\odot} \text{ yr}^{-1}$)	$\text{SFR}_{\text{CMZ,00m}}$ Herschel Temp ($M_{\odot} \text{ yr}^{-1}$)	$\text{SFR}_{\text{CMZ,00m}}$ 50 K ($M_{\odot} \text{ yr}^{-1}$)	Best SFR Estimate [*] ($M_{\odot} \text{ yr}^{-1}$)	Required Ext P/k_{B} (K cm^{-3})	Parent Tot P/k_{B} (K cm^{-3})	Pressure Ratio	Confined
Branches																
G0.720-0.069	8	1.40E+08	2.20E+03	6.10E+07	1.70E+03	2.10E+08	3.50E-02	3.50E-02
G0.750-0.070	9	1.20E+08	2.30E+03	4.90E+07	1.70E+03	1.70E+08	3.00E-02	3.00E-02
G0.970-0.067	11	5.90E+07	1.70E+03	1.40E+07	8.80E+02	7.30E+07	1.30E-02	1.30E-02
G0.840-0.065	12	5.10E+07	2.10E+03	1.20E+07	8.60E+02	6.40E+07	1.10E-02	1.10E-02
G0.830-0.062	13	4.90E+07	2.20E+03	1.20E+07	8.60E+02	6.10E+07	1.00E-02	1.00E-02
G0.820-0.059	14	4.00E+07	2.30E+03	8.50E+06	7.90E+02	4.90E+07	8.40E-03	8.40E-03
G0.800-0.060	15	3.30E+07	2.60E+03	6.50E+06	7.70E+02	4.00E+07	6.80E-03	6.80E-03
G359.900-0.071	19	4.70E+07	4.70E+03	2.50E+07	3.00E+03	7.20E+07	1.20E-02	1.20E-02
G0.020-0.058	27	3.60E+07	5.20E+03	1.90E+07	3.60E+03	5.40E+07	9.30E-03	9.30E-03
G1.610-0.059	23	3.60E+06	5.50E+02	3.60E+06	6.20E-04	6.20E-04
G0.670-0.059	17	2.40E+07	3.90E+03	4.90E+06	8.10E+02	2.90E+07	4.90E-03	4.90E-03
G0.040-0.054	31	2.70E+07	5.80E+03	1.30E+07	4.10E+03	4.00E+07	6.90E-03
G0.650-0.040	25	1.90E+07	4.70E+03	3.40E+06	8.80E+02	2.20E+07	3.80E-03
G1.040-0.051	29	4.80E+06	1.40E+03	5.90E+05	4.80E+02	5.40E+06	9.40E-04
G359.530-0.120	18	9.30E+06	3.60E+03	4.90E+06	1.90E+03	1.40E+07	2.40E-03
G0.670-0.038	26	1.30E+07	5.40E+03	2.00E+06	8.50E+02	1.50E+07	2.50E-03
G359.960-0.078	32	1.30E+07	5.80E+03	6.90E+06	3.90E+03	2.00E+07	3.40E-03
G0.660-0.023	37	7.90E+06	7.10E+03	1.10E+06	9.80E+02	8.90E+06	1.50E-03
G0.210-0.003	44	5.60E+06	5.10E+03	2.90E+06	4.20E+03	8.50E+06	1.50E-03
G359.910-0.079	34	6.80E+06	6.30E+03	3.10E+06	3.60E+03	9.90E+06	1.70E-03
G0.220-0.490	3	2.10E+05	3.70E+02	2.80E+05	6.60E+02	4.90E+05	8.50E-05
G0.110-0.079	35	1.70E+06	4.00E+03	1.60E+06	4.40E+03	3.30E+06	5.70E-04
G0.400+0.048	50	8.50E+05	3.30E+03	1.90E+05	7.60E+02	1.00E+06	1.80E-04
Leaves																
G359.510-0.130	24	4.50E+06	3.90E+03	2.20E+06	1.90E+03	6.70E+06	1.20E-03	7.89E-01	7.70E-03	7.70E-03	2.80E+07	8.00E+07	2.88	Y
G1.070-0.049	33	1.50E+06	1.40E+03	3.80E+04	4.20E+02	1.60E+06	2.70E-04	5.94E-01	4.90E-03	7.10E-03	1.10E-03	7.10E-03	2.20E+07	1.80E+08	8.23	Y
G0.230-0.004	45	4.10E+06	5.10E+03	2.70E+06	4.20E+03	6.80E+06	1.20E-03	6.40E-01	9.50E-03	9.50E-03	6.80E+08	2.70E+08	0.40	N
G0.890-0.044	39	1.30E+06	1.80E+03	3.40E+05	4.70E+02	1.60E+06	2.80E-04	5.39E-01	5.40E-03	5.40E-03	3.00E+07	1.80E+08	6.10	Y
G0.820-0.190	21	1.30E+06	2.10E+03	2.80E+05	4.50E+02	1.60E+06	2.80E-04	5.26E-01	5.60E-03	5.60E-03	1.90E+08	5.10E+08	2.63	Y
G1.720-0.390	6	1.50E+05	2.70E+02	1.50E+05	2.60E-05	7.20E-01	1.00E-03	1.00E-03
G0.670-0.028	43	4.90E+06	9.60E+03	4.70E+05	9.50E+02	5.40E+06	9.20E-04	2.11E-01	2.60E-02	2.60E-02	-5.10E+08	2.40E+09	...	SG
G0.720-0.090	30	1.90E+06	3.90E+03	3.00E+05	6.00E+02	2.20E+06	3.90E-04	3.98E-01	8.70E-03	1.40E-02	2.70E-03	1.40E-02	9.70E+08	1.50E+09	1.51	Y
G359.690-0.130	28	1.40E+06	2.90E+03	7.70E+05	1.60E+03	2.20E+06	3.70E-04	7.44E-01	4.70E-03	4.70E-03	5.10E+07	1.40E+08	2.76	Y
G359.880-0.081	36	1.90E+06	5.10E+03	8.50E+05	2.40E+03	2.80E+06	4.80E-04	3.33E-01	1.20E-02	5.10E-02	9.20E-03	9.20E-03	2.00E+08	4.60E+08	2.26	Y
G1.020-0.230	16	4.20E+05	1.10E+03	8.40E+04	5.30E+02	5.00E+05	8.60E-05	7.05E-01	2.20E-03	2.20E-03	3.40E+08	1.60E+08	0.47	N
G0.550-0.870	0	6.10E+05	1.80E+03	6.10E+05	1.10E-04	6.33E-01	2.70E-03	2.70E-03
G359.600-0.220	20	8.60E+05	2.70E+03	4.80E+05	1.50E+03	1.30E+06	2.30E-04	5.74E-01	4.60E-03	4.60E-03	1.60E+09	8.00E+07	0.05	N
G0.240-0.470	5	1.10E+05	4.00E+02	1.90E+05	6.70E+02	3.00E+05	5.20E-05	7.04E-01	1.60E-03	1.60E-03
G0.490+0.008	48	1.00E+06	4.00E+03	1.80E+05	7.10E+02	1.20E+06	2.10E-04	3.07E-01	8.20E-03	1.70E-02	2.90E-03	1.70E-02	2.20E+08	8.10E+08	3.75	Y
G0.120+0.003	46	1.20E+06	5.00E+03	1.20E+06	2.10E-04	5.32E-01	4.70E-03	1.70E-03	5.00E-04	1.70E-03	1.20E+08	2.70E+08	2.23	Y
G1.600+0.012	47	1.50E+05	6.80E+02	1.50E+05	2.60E-05	3.73E-01	2.00E-03	5.00E-03	5.00E-04	5.00E-03	1.60E+08	6.60E+07	0.42	N
G1.650-0.052	42	1.10E+05	5.20E+02	1.10E+05	1.90E-05	3.73E-01	1.60E-03	1.50E-03	2.00E-04	1.50E-03	3.20E+07	6.60E+07	2.06	Y
G359.940+0.160	54	1.70E+05	9.20E+02	1.60E+05	8.20E+02	3.30E+05	5.70E-05	6.06E-01	1.90E-03	1.90E-03	1.60E+09	8.30E+07	0.05	N
G0.330-0.190	22	2.90E+05	1.80E+03	3.20E+05	2.20E+03	6.00E+05	1.00E-04	6.28E-01	2.70E-03	2.70E-03
G3.430-0.350	10	5.50E+04	3.30E+02	5.50E+04	9.50E-06	5.83E-01	6.90E-04	6.90E-04
G0.200-0.520	4	5.40E+04	3.40E+02	1.50E+04	4.70E+02	6.90E+04	1.20E-05	5.77E-01	7.90E-04	7.90E-04
G0.410+0.048	51	4.00E+05	3.20E+03	7.90E+04	6.50E+02	4.80E+05	8.20E-05	3.28E-01	4.50E-03	2.70E-03	5.00E-04	2.70E-03	2.80E+08	2.80E+08	1.03	Y
G359.980-0.071	41	9.10E+05	8.30E+03	4.10E+05	5.50E+03	1.30E+06	2.30E-04	2.79E-01	9.40E-03	6.30E-03	1.80E-03	6.30E-03	3.60E+08	4.60E+08	1.28	Y
G0.340+0.060	53	3.50E+05	3.50E+03	1.20E+05	1.20E+03	4.70E+05	8.10E-05	4.14E-01	3.50E-03	3.50E-03	3.70E+08	1.90E+08	0.51	N

Table 3
(Continued)

Name	ID	L_{tot} (Cool) (L_{\odot})	$\langle L \rangle$ (Cool) ($L_{\odot} \text{ pix}^{-1}$)	L_{tot} (Warm) (L_{\odot})	$\langle L \rangle$ (Warm) ($L_{\odot} \text{ pix}^{-1}$)	L_{totalIR} (L_{\odot})	$\text{SFR}_{\text{totalIR}}$ ($M_{\odot} \text{ yr}^{-1}$)	t_{ff} (Myr)	SFR_{FF} ($M_{\odot} \text{ yr}^{-1}$)	$\text{SFR}_{\text{CMZoom}}$ Herschel Temp ($M_{\odot} \text{ yr}^{-1}$)	$\text{SFR}_{\text{CMZoom}}$ 50 K ($M_{\odot} \text{ yr}^{-1}$)	Best SFR Estimate ($M_{\odot} \text{ yr}^{-1}$)	Required Ext P/k_{B} (K cm^{-3})	Parent Tot P/k_{B} (K cm^{-3})	Pressure Ratio	Confined
G0.120-0.081	38	4.30E+05	4.30E+03	3.60E+05	3.60E+03	7.90E+05	1.40E-04	3.12E-01	6.30E-03	4.00E-04	1.00E-04	4.00E-04	2.30E+08	1.90E+08	0.83	N
G358.460-0.390	7	3.80E+04	4.70E+02	3.80E+04	6.60E-06	4.72E-01	7.00E-04	7.00E-04
G356.660+0.560	56	1.80E+03	3.00E+01	1.80E+03	3.20E-07	5.28E-01	2.00E-04	2.00E-04
G0.070-0.076	40	2.20E+05	3.80E+03	2.90E+05	6.40E+03	5.10E+05	8.80E-05	2.50E-01	6.10E-03	6.40E-03	1.50E-03	6.40E-03	3.50E+08	1.90E+08	0.54	N
G0.090-0.660	2	2.80E+04	5.30E+02	2.80E+04	4.80E-06	4.65E-01	6.10E-04	6.10E-04
G0.380+0.050	52	1.70E+05	3.70E+03	3.70E+04	8.00E+02	2.10E+05	3.60E-05	2.74E-01	3.30E-03	3.90E-02	1.00E-02	1.00E-02	1.80E+09	2.80E+08	0.15	N
G356.520+0.210	55	1.80E+03	4.70E+01	1.80E+03	3.20E-07	4.65E-01	2.30E-04	2.30E-04
G357.070-0.770	1	3.50E+02	1.30E+01	3.50E+02	6.00E-08	4.30E-01	6.00E-08
G0.650+0.030	49	1.10E+05	3.80E+03	1.20E+04	3.90E+02	1.30E+05	2.20E-05	1.64E-01	4.10E-03	4.10E-03	1.50E+09	2.40E+09	1.65	Y

Note. Shown for each structure is the source name, structure ID, total luminosity and mean luminosity for the cool and warm components, respectively, the combined total IR luminosity, the SFR inferred from that total IR luminosity assuming the star-forming relation from R. C. Kennicutt (1998), the freefall time, the SFR estimated using the method from A. T. Barnes et al. (2017) but using the freefall time, the SFR reported in matching sources from the CMZoom catalog (H. P. Hatchfield et al. 2024), the best overall SFR estimate for each structure, the external pressure requirement for confinement, the total pressure of the parent structure in the dendrogram, the ratio of the total parent pressure/required external pressure, and whether a leaf is confined by the pressure of its parent structure (Yes/No/Self-gravitating). The grouping and order of structures is the same as in Table 1. *See Section 3.5 for details regarding the choice of best SFR estimate. No best SFR estimate is given for branches with $A < 1000 \text{ pc}^{-2}$.

Table 4
Power-law Fits to the Column Density PDFs of Various CMZ Regions

Region Name	ID	Name	$x_{\min} = N(\text{H}_2)$ (cm^{-2})	PL Slope α	PL Error 1σ	Best SFR Estimate ($M_{\odot} \text{yr}^{-1}$)	SFR Method	
SgrB2		Overall	1.7e+23	-2.5	0.1	
	21	M0.8-0.2 ring	9.5e+22	-8.4	0.5	5.6e-3	freefall	
	43	SgrB. Main	... ^a	2.6e-2	freefall	
	30	SgrB2 extended	1.4e+23	-8.8	0.5	1.4e-2	CMZoom	
	48	Clouds e/f	1.2e+23	-3.6	0.2	1.7e-2	CMZoom	
Inner 100 pc		Overall	7.2e+22	-3.3	0.1	
	24	SgrC	7.7e-3	freefall	
	45	Brick plus	9.5e-3	freefall	
	36	20 km s ⁻¹ cloud	9.2e-3	CMZoom 50 K	
	46	Dust Ridge Bridge	6.0e+22	-5.9	0.6	1.7e-3	CMZoom	
	51	Cloud D	2.7e-3	CMZoom	
	41	50 km s ⁻¹ cloud	9.5e+22	-5.0	0.4	6.3e-3	CMZoom	
	53	Cloud b	3.5e-3	freefall	
	38	Straw and Sticks Clouds	8.2e+22	-7.6	0.7	4.0e-4	CMZoom	
	40	Stone Cloud	6.4e-3	CMZoom	
	52	Cloud c	1.0e-2	CMZoom 50 K	
	Outer 100 pc		Overall	1.0e+23	-7.3	0.2
		23	1.6 complex	6.2e+22	-4.9	0.1	6.2e-4	total IR
29		1.1 complex	9.5e+22	-7.6	0.3	...	none	
33		1.1 East	8.7e+22	-6.5	0.2	7.1e-3	CMZoom	
39		1.1 West	9.5e+22	-8.9	0.5	5.4e-3	freefall	
47		1.6 North	8.8e+22	-5.5	0.4	5.0e-3	CMZoom	
42		1.6 South	1.0e+23	-6.8	0.5	1.5e-3	CMZoom	

Notes. We include here power-law fits to both the overall Sgr B2, inner 100 pc, and outer 100 pc regions highlighted in Figure 3 as well as fits to individual dendrogram structures shown in Figures 4, 5, and 6. These are maximum likelihood estimator (MLE) fits where the lower-limit of the fit is automatically determined by the algorithm, and reported here as x_{\min} . More details can be found in Section 3.6.

^a Structures that involve power-law fits to fewer than 50 data points or poor overall fits (Section 3.6) and that are excluded.

HCN 1 – 0 ($F = 2-1$) at 88.6318473 GHz, and HC₃N 10 – 9 at 90.978989 GHz. These molecular line transitions tell us different things about the molecular gas. This combination was chosen to represent both the variation in properties one expects, as well as for comparison with lines observed in other regions.

We first extract an integrated spectrum for each line over each dendrogram structure mask. We compute the moment 0 (integrated value), moment 1 (the intensity weighted velocity), and moment 2 (intensity weighted velocity dispersion) of the integrated spectra for each line. In Table 2 we report these values. In the case of the moment 2 values, we have converted from the native velocity dispersion σ to the equivalent FWHM for a Gaussian line profile.

The CMZ is a complex region, both kinematically and chemically, with emission from different regions along many lines of sight. For example, Figure 1 shows the HC₃N spectra for structures 46 and 36 (the Dust Ridge Bridge and the 20 km s⁻¹ cloud). While structure 36 (20 km s⁻¹ cloud) shows a single wide, somewhat asymmetric spectral line centered around 18 km s⁻¹, structure 46 (Dust Ridge Bridge) shows one strong peak centered at about 55 km s⁻¹ that dominates the moment calculation and a second small peak around -30 km s⁻¹. This likely indicates that structure 46 contains gas from more than one line-of-sight location in the CMZ, while structure 36 is a single cloud structure that is well suited to moment analysis. This complexity is well documented in, e.g., J. D. Henshaw et al. (2016a), R. Shetty et al. (2012), and J. Kauffmann et al. (2017a), who performed more comprehensive kinematic analyses of gas in the CMZ.

Our approach of using moment analysis is chosen to enable study of the entire CMZ hierarchy in a consistent and simple way. It enables comparison with other integrated structure moment analysis works from Milky Way and extragalactic observations, which we show in Section 4.2. The third paper in this series, Paper III, carefully and systematically refines this catalog into well-defined molecular clouds in position–position–velocity space. Paper III performs a detailed kinematic analysis of each of these clouds, including multiple component Gaussian fitting using pyspeckit, which implements the Levenberg–Marquardt algorithm.

3.4. Luminosities of CMZ Structures

In Paper I of this series, we computed modified blackbody fits at each source pixel within the inner $\ell = 40^\circ$ of the Galaxy. In fitting a single-component modified blackbody function to each position, we assumed that the dust emission was well fit by a single temperature component. The wavelengths included in the fits were 160, 250, 350, and 500 μm , thereby making this measurement most sensitive to relatively “cool” dust (~ 20 K). We integrate underneath the modified blackbody fit at each source pixel to generate a “cool” far-IR luminosity map of the region. We then integrate the luminosity values in this map over each of our Herschel dendrogram structure masks and report an integrated as well as structure average “cool” luminosity in Table 3.

In one of our earlier papers, A. T. Barnes et al. (2017), we performed two temperature component modified blackbody fits in the inner 2° longitude and 1° latitude of the Galaxy. In these

fits, we also incorporated shorter wavelength data from Spitzer, making these measurements more sensitive to an additional “warm” component of the dust. Since A. T. Barnes et al. (2017) used the same background-subtraction method as this work, we use the “warm” IR dust component map from A. T. Barnes et al. (2017) to calculate and report a total and average “warm” IR luminosity for each dendrogram structure in Table 3. We note that since the two-component “warm” temperature component analysis was only performed in the inner 2° longitude and 1° latitude of the Galaxy, structures outside these boundaries (including if only part of the structure is outside the boundary) are excluded in the “warm” luminosity column in the Table.

In Table 3 we report both the “cool” and “warm” IR luminosities for each structure. Additionally, we add together these two luminosity components for each structure and report the total IR luminosity.

3.5. Estimates of the Star Formation Rates of CMZ Structures

We estimate SFRs in each CMZ structure. We implement three different methods to do this that are most relevant on different size scales. The first is using the total IR luminosity and can be applied to only the largest structures in our sample. The second two are intended to be used on individual molecular clouds in the CMZ. Each method is described in more detail below.

Building upon the work from A. T. Barnes et al. (2017), we use the total IR luminosity calculated in Section 3.4 to estimate a total SFR for each structure by implementing the conversion factor from R. C. Kennicutt (1998) of 4.5×10^{-44} L (TIR) $\text{erg s}^{-1} M_\odot^{-1} \text{yr}$. This value is reported in Table 3.

While using the total IR luminosity is a common method to estimate global SFRs on large scales, this calibration assumes a large and complete stellar population with regions in a range of evolutionary states and is not valid for the smaller structures in our sample. Additionally, it assumes that the total IR for each structure is produced by internal heating, which is not the case for some CMZ molecular clouds, such as the “Brick,” which is predominantly heated by the external radiation field. Therefore, we implement two additional methods to estimate SFRs for the small structures in our sample. These methods are described below. In our analysis in this paper, we only utilize the global SFR estimates from total IR luminosity for branches in our catalog with a total structure surface area of 1000 pc^2 or greater. This cutoff is driven by the idea that on scales of $>1 \text{ kpc}$, one can generally assume a complete stellar population in a variety of evolutionary stages, so this SFR estimate should be valid for structures larger than 1000 pc^2 (R. C. Kennicutt 1998). A. T. Barnes et al. (2017) compared this total IR luminosity SFR in the entire CMZ with other measures of the SFR based on IR luminosity, YSO counting, and free-free emission and find overall good agreement, better than 50% in all but one potentially problematic case (F. Yusef-Zadeh et al. 2009; see also C. M. Koepferl et al. 2015).

We estimate SFRs for the smaller-scale structures in our catalog using two methods. The first method is to use the SFRs derived by H. P. Hatchfield et al. (2024). H. P. Hatchfield et al. (2024) estimated SFRs in regions observed with the CMZoom Survey (C. Battersby et al. 2020) by first combining archival data and catalogs of star formation tracers, such as mid-IR point sources, methanol masers, UCHII regions, to identify which of the 285 high-robustness CMZoom leaves

from H. P. Hatchfield et al. (2020) is actively engaged in the star formation process. Each leaf is then given a designation of either “robustly” or “ambiguously” star-forming as described in H. P. Hatchfield et al. (2024). The mass of each star-forming leaf is divided by its freefall time, multiplied by an estimated star formation efficiency ($\text{SFE} = 0.25 \pm 0.15$ is assumed in H. P. Hatchfield et al. 2024) and corrected for the low-mass star formation to which the CMZoom survey is not sensitive (see extensive details in H. P. Hatchfield et al. 2024). The total SFR of each cloud in CMZoom is then the summation of the SFRs of each star-forming leaf in the cloud. For this paper, we use the CMZoom SFRs for both robustly and ambiguously star-forming sources (Table 3 in H. P. Hatchfield et al. 2024). We report the CMZoom SFR estimates for both the Herschel temperature calculation (usually around 20 K) as well as the CMZoom SFR estimate assuming a uniform temperature of 50 K. The former is the better assumption in a quiescent cloud, while the latter better captures the true mass, and therefore SFR for a warm, actively star-forming cloud.

In order to utilize the SFRs calculated in H. P. Hatchfield et al. (2024), we performed a manual comparison of each of our structures with the CMZoom clouds and found that only 12 regions had very good overlap and could be fairly compared side-by-side. For these 12 regions, we include the CMZoom SFR estimates using both robustly and ambiguously star-forming sources. Since H. P. Hatchfield et al. (2024) involved a careful and thorough examination of multiwavelength data of all of the CMZoom regions, 12 of which overlap with our hierarchical catalog, we consider this estimate of the SFR to be the most reliable. Therefore, when it is available, this estimate is used in the final column of Table 3 indicating it is the best available SFR. By default, we use the CMZoom SFR estimate using the Herschel temperature, however, for two highly active star-forming regions (cloud c: G0.380+0.050 and the 20 km s^{-1} cloud: G359.880-0.081), we use the 50 K CMZoom SFR estimate, as discussed in more detail at the end of this section. Both estimates are included in Table 3.

For the second method of calculating SFRs in the smaller structures in our catalog, we follow the method presented in A. T. Barnes et al. (2017). We summarize the method here, but refer the reader to that work for further details. First, in order to calculate the total embedded stellar mass, we assume that the total IR luminosity for each cloud is a result of the reprocessed bolometric luminosity of the embedded stars within each cloud, which is then dominated by the single most-massive star (i.e., $M \propto L^x$, where $x \sim 1-3.5$; J. R. Mould 1982; M. Salaris & S. Cassisi 2005). This is a reasonable assumption in an actively star-forming cloud. In cases where external radiation is a significant contributor to the luminosity, our values set an upper limit of the possible SFR. To convert from a luminosity to the mass of the embedded object ($M_{*,\text{tot}}$), we use the conversions from B. Davies et al. (2011). As in A. T. Barnes et al. (2017), we then extrapolate a total embedded stellar mass ($M_{*,\text{tot}}$) from the most-massive star in the system by solving for the normalization β in the following two equations:

$$1 = \beta \int_{M_{*,\text{max}}}^{\infty} m^{-\alpha} dm, \quad (1)$$

where $\alpha = 2.3$ and,

$$M_{*,\text{tot}} = \beta \int_{0.001}^{\infty} m^{1-\alpha} dm, \quad (2)$$

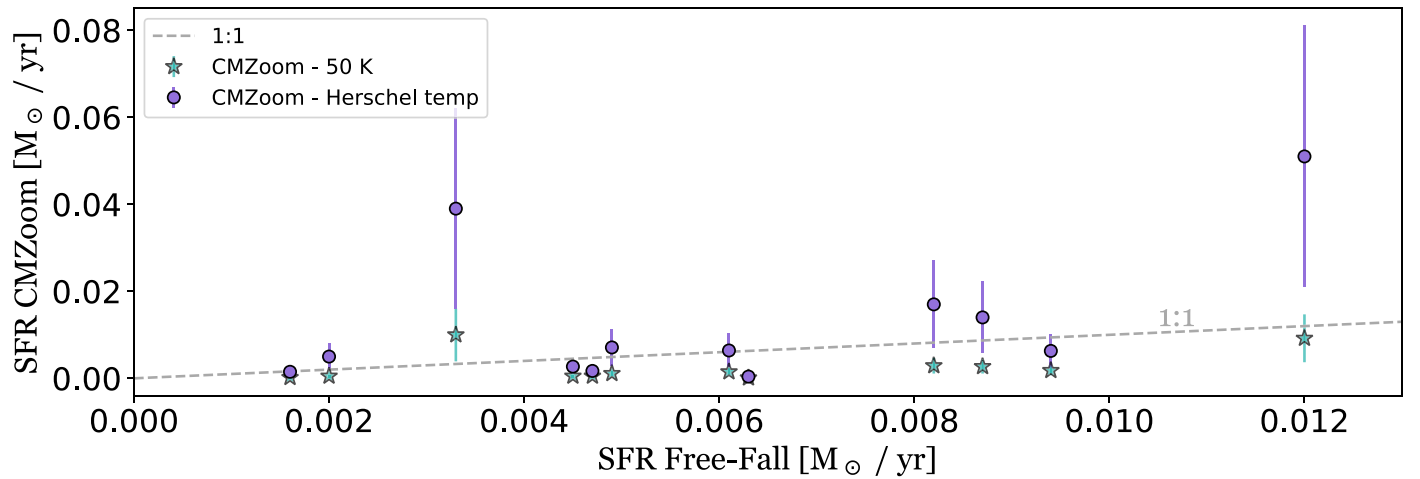


Figure 2. A comparison between the SFRs calculated from CMZoom (H. P. Hatchfield et al. 2024, shown on the y-axis) and using the freefall method (this work in Section 3.5, based on A. T. Barnes et al. 2017, shown on the x-axis) shows generally good agreement in the 12 sources for which both measurements are available. The dashed gray line shows the 1:1 line. The purple circles show the SFR estimates from CMZoom assuming the Herschel-calculated dust temperature (our default SFR choice), while the green stars from CMZoom assume a higher dust temperature of 50 K (H. P. Hatchfield et al. 2024). Including their 1σ error bars, most of the points agree with the 1:1 line, with two clear outliers that have much higher CMZoom estimated SFRs than their freefall estimates. From left to right in this plot, the two high outliers are cloud c (G0.380+0.050) and the 20 km s⁻¹ cloud (G359.880-0.081). These two regions are actively star-forming, so the 50 K SFR estimate from CMZoom is likely more appropriate (see Section 3.5) and is therefore used in Table 3 and agrees better with the freefall SFR estimate. The very low outlier is the Straw and Sticks clouds (ID: 38). Table 3 reports all calculated SFRs for each source and also indicates in the final column the best available SFR, which is discussed in more detail in Section 3.5.

where $\alpha = 0.3$ for $0.001 < m/M_{\odot} < 0.08$, $\alpha = 1.3$ for $0.08 < m/M_{\odot} < 0.5$, and $\alpha = 2.3$ for $m/M_{\odot} > 0.5$, as in the initial mass function from P. Kroupa (2001).

Now that we have a total embedded stellar mass for each cloud, we need a timescale over which these stars are forming. A. T. Barnes et al. (2017) used the estimated time since pericenter passage for this timescale, which they assumed corresponded to the initiation of star formation in the cloud. By dividing the total embedded stellar mass by the time since star formation began, A. T. Barnes et al. (2017) estimated cloud-by-cloud SFRs. We instead use the calculated freefall time for each cloud as the timescale for star formation. We calculate this freefall time (t_{ff}) using the structure mass (M), radius (R), and density (n) from Table 1 and the standard freefall time expression:

$$t_{ff} = \sqrt{\frac{3\pi}{32G\rho}}, \quad (3)$$

where G is the gravitational constant, and $\rho = M/\frac{4}{3}\pi R^3$. We then divide the total embedded stellar mass ($M_{*,tot}$) by the freefall time to calculate the freefall SFR (SFR FF) reported in Table 3. The calculated freefall times are also reported in Table 3.

All of the SFRs are reported in Table 3. The total IR estimate is considered valid in structures larger than 1000 pc², but otherwise is not reliable. For the overall dense CMZ (structure ID: 9), we find a total IR SFR estimate of $0.03 M_{\odot} \text{ yr}^{-1}$. Unsurprisingly, this is lower than the estimate for the full inner region of the Galaxy from A. T. Barnes et al. (2017) of $0.07 M_{\odot} \text{ yr}^{-1}$ because the area covered is substantially lower and is focused on dense gas, missing the bright radiation in the more diffuse ISM responsible for much of the total IR luminosity. When we compare the total IR SFR estimate against either of the two cloud-scale methods, the total IR SFR estimate vastly underpredicts the SFR in a single cloud. This is not surprising since it assumes that the luminosity comes from

star formation spanning many spatial and timescales, which is not a valid assumption on the cloud scale.

The two cloud-by-cloud SFR estimates are considered to be reliable within leaves that generally represent individual molecular clouds. In general, the SFRs from the CMZoom and freefall methods match each other quite well, however, this is not necessarily surprising since they both rely on the freefall timescale in their calculations. A comparison of the 12 points with overlapping estimates from these two methods is shown in Figure 2, with the CMZoom-based SFR estimates from H. P. Hatchfield et al. (2024) on the y-axis and the freefall based method derived in this work, based on the work from A. T. Barnes et al. (2017) on the x-axis. For each point, we include a 1σ error bar. We compare the relationship between these SFR estimates and inspect their distance from the 1:1 line (dashed line). Most of the Herschel temperature points (our default assumption) are within 1σ of the 1:1 line. However, there are two notable exceptions. There are two regions with significantly higher CMZoom SFRs than the freefall estimate: cloud c (G0.380+0.050) and the 20 km s⁻¹ cloud (G359.880-0.081). These clouds have CMZoom SFRs of 38.7 and $50.6 \times 10^{-3} M_{\odot} \text{ yr}^{-1}$, respectively, and freefall SFRs of 3.3 and $12 \times 10^{-3} M_{\odot} \text{ yr}^{-1}$, a large discrepancy. These two regions are known to contain active star formation (e.g., X. Lu et al. 2019a, 2019b; H. P. Hatchfield et al. 2024). Therefore, we select the CMZoom 50 K SFRs (see H. P. Hatchfield et al. 2024, for details) as the better SFR estimate in Table 3 for these two clouds. Then, we have CMZoom SFRs of 10.2 and $9.2 \times 10^{-3} M_{\odot} \text{ yr}^{-1}$, respectively, showing much better agreement between our freefall SFR estimates and the CMZoom 50 K SFR estimates for these two active star-forming regions. There is also one low outlier (low CMZoom SFR) compared with the freefall method in this plot, which is the Straw and Sticks clouds (ID: 38), for which we can offer no simple explanation except that these methods are imperfect and the agreement within 1σ for the majority of points should perhaps instead be the surprise.

In the final column of Table 3 we report what we consider to be the best SFR estimate for each structure. For branches $>1000 \text{ pc}^2$ in size, this is the total IR SFR estimate. For leaves, this is the CMZoom-based estimate from H. P. Hatchfield et al. (2024) where available and the freefall based estimate from this work in other cases. Based on the discussion in the previous paragraph, we use the 50 K CMZoom SFR estimate for two clouds, cloud c (G0.380+0.050) and the 20 km s^{-1} cloud (G359.880-0.081), and otherwise use the standard ‘‘Herschel temperature’’ CMZoom SFR as the best SFR. Branches that are smaller than 1000 pc^2 do not have a best SFR estimate. These best SFR estimates are used for the remainder of this work.

There is substantial uncertainty in any measure of SFR, with many assumptions and caveats. In each of our leaves with a CMZoom or freefall SFR estimate, we also have a total IR estimated SFR. The total IR estimated SFR is substantially lower than the CMZoom or freefall SFR estimates. However, the total IR SFR relations were calibrated over large areas with stars in a range of evolutionary stages (e.g., R. C. Kennicutt & N. J. Evans 2012) and are therefore not applicable to single molecular clouds bound by external pressure. When we focus in on the very densest gas, much of which is actively engaged in the star formation process already (e.g., X. Lu et al. 2021; D. L. Walker et al. 2021), we would expect the SFR to be higher. The freefall times reported in Table 3 of the order of 0.1–0.8 Myr are a reasonable estimate for expected timescales for high-mass star formation (C. Battersby et al. 2017). Focused future efforts on calibrating SFR prescriptions from galaxy to cloud scales is of great importance.

3.6. Creating and Fitting Probability Distribution Functions

Column density probability distribution functions (N-PDFs) provide a simplified view of the structure in a region that can be easily compared over different physical regions or between simulations and observations. Therefore, N-PDFs are widely used and discussed in the literature. We compute simple N-PDFs for the column density maps from Paper I and fit a simple power law (details to follow), as well as perform comparisons with literature values. However, we caution the reader that there exists substantial complexity in the underlying N-PDF of any star-forming region (e.g., H. H.-H. Chen et al. 2018) as well as in the observational extraction of a single number (e.g., a power-law slope) from these complex data (e.g., J. Alves et al. 2017).

Simulations of isothermal, supersonic turbulence predict a lognormal N-PDF (e.g., E. C. Ostriker et al. 2001; J. Ballesteros-Paredes et al. 2011; P. Padoan & Å. Nordlund 2011; P. Hennebelle & E. Falgarone 2012; C. Federrath & R. S. Klessen 2013) and when self-gravity is introduced, there exists a power-law tail at high densities (e.g., R. S. Klessen 2000; C. Federrath et al. 2008; J. Kainulainen et al. 2009; P. Girichidis et al. 2014). B. Burkhart et al. (2017) presented an analytic expression for the expected transition point between the two functions. N-PDFs offer the tantalizing prospect of allowing for measurements of a number of physical parameters (such as turbulent driving and Mach number). Many observational studies have reported a lognormal N-PDF at low to moderate column densities with a possible power-law tail at high column densities, particularly in the presence of star formation (e.g., J. Kainulainen et al. 2009; N. Schneider et al. 2013; J. M. Rathborne et al. 2014; J. Abreu-Vicente et al. 2015; N. Schneider et al. 2016, 2022). However, work by

M. Lombardi et al. (2015) and J. Alves et al. (2017) suggests that observed molecular cloud N-PDFs are consistent with power laws and previous interpretations of a lognormal nature may be due to observational completeness biases (note alternative view of V. Ossenkopf-Okada et al. 2016).

In this work, we fit N-PDFs to data within closed column density contours to ensure completeness (J. Alves et al. 2017). We identify the lowest closed column density contour that allows for natural separation into key CMZ regions as $N(\text{H}_2) = 6 \times 10^{22} \text{ cm}^{-2}$. Using this column density threshold, we divide the CMZ into three regions: $R < 100 \text{ pc}$ ($0.4 \gtrsim \ell \gtrsim -0.6$), SgrB2 ($0.8 \gtrsim \ell \gtrsim 0.4$), and $R > 100 \text{ pc}$ ($1.8 \gtrsim \ell \gtrsim 0.8$), with the exact regions shown as contours in Figure 3. These are the same regions as in Paper I, Section 4.2. The N-PDFs for the CMZ overall and for each region are shown in the bottom panels of Figure 3.

We further investigate the nature of N-PDFs within each of these key CMZ regions by studying the N-PDFs of select individual dendrogram structures, which have already been identified as described in Section 2.2. For consistency, we plot and fit these dendrogram structures above the same column density threshold as the larger regions, $N(\text{H}_2) = 6 \times 10^{22} \text{ cm}^{-2}$, or their individual complete column density limit, whichever is higher. We present the three Figures 4, 5, and 6 to show the location of each of these selected dendrogram structures on a map and within the dendrogram tree hierarchy. These figures also show the N-PDF of the overall CMZ region in which they are located and the N-PDFs of the individual substructures in the bottom panels. While there are a handful of saturated pixels in the Herschel map toward SgrB2, they are very few and do not affect the fits or analysis.

We choose to fit only the high-column density portion of the N-PDFs, which is what we see above these complete closed column density contours. This portion of the N-PDF is generally considered to correspond to the star-forming gas in the cloud (e.g., N. Schneider et al. 2016, 2022). While there are many differing opinions on the choice of power-law fits versus lognormal fits, we choose to fit simple power laws to this high-column density gas, which allows for a simple, uniform fit to all of the data in our sample, and facilitates region inter-comparison. While lower column density material may require a lognormal function (or very steep power law), fits to this material are more challenging to constrain observationally since they correspond to dimmer emission, often near the noise limit of observations, and are often subject to incomplete column density cuts (see, e.g., J. Alves et al. 2017). For this work, we focus on simple power-law fits to the high-column density N-PDFs in the CMZ.

We fit the high-column density slopes of the N-PDFs using a maximum likelihood estimator (MLE) method that produces a robust measurement of the slope that does not depend on choice of bin size. We fit a power law of the form:

$$p(N) = CN^\alpha \quad (4)$$

where p is the probability density, N is the column density, α is the power-law index slope, and C is a constant. We use the python package POWERLAW²³ from J. Alstott et al. (2014), which relies upon statistical methods described in A. Clauset et al. (2009) and A. Klaus et al. (2011), often used in astronomy

²³ <https://github.com/jeffalstott/powerlaw>

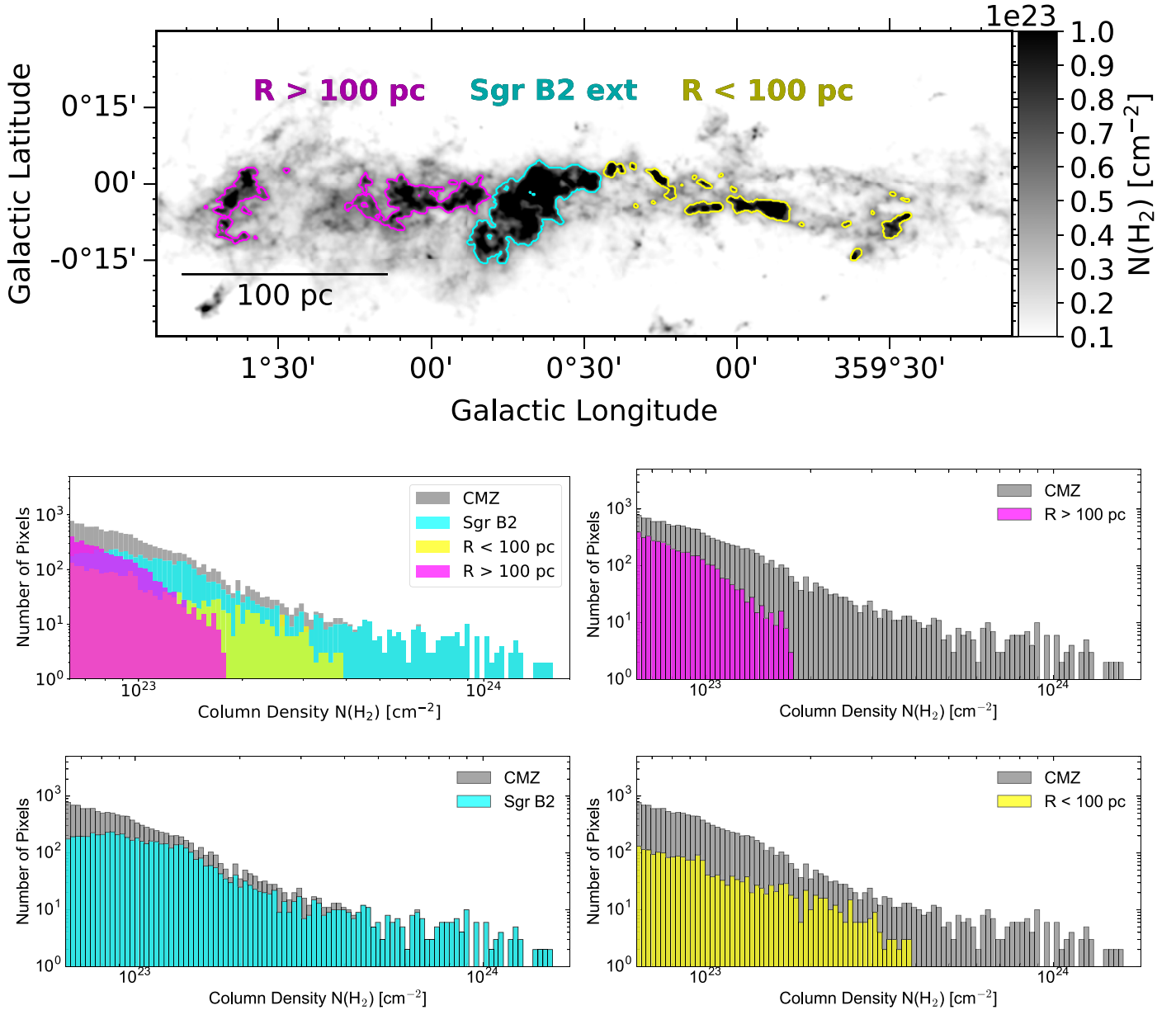


Figure 3. Column density PDFs for various regions in the CMZ highlight that most of the highest column density gas in the CMZ comes from the SgrB2 region, which has a very shallow slope, followed by the $R < 100$ pc region, which has the highest fraction of low column density gas and steepest power-law slope. As described in Section 3.6, we used a minimum column density threshold of $N(\text{H}_2) = 6 \times 10^{22} \text{ cm}^{-2}$ to separate the CMZ into these three key regions. The column density map is shown on top, and the three regions are highlighted in color contours. The colors correspond to the PDFs in the plot below, while the gray shows the PDF over the entire CMZ above the same column density threshold. Each of these region PDFs is broken into select individual dendrogram structures in Figures 4, 5, and 6.

(e.g., T. V. Veltchev et al. 2019). This approach combines maximum-likelihood fitting methods and goodness-of-fit tests based on the Kolmogorov–Smirnov (K-S) statistic and likelihood ratio.

The POWERLAW package automatically determines an “ x_{\min} ” above which to fit the power-law slope and then fits a simple power law (Equation (4)) above this value. In many cases, this x_{\min} value is above the lowest closed column density contour, which means that the material below the x_{\min} column density is not well represented by the same power law, i.e., there is some truncation, either physical or observational, that causes a turnover. The POWERLAW algorithm accomplishes this by measuring the maximum-likelihood alpha parameter for each possible value of x_{\min} , then finds the x_{\min} that provides the

closest match based on the K-S test. The results of these fits are shown in Table 4 as well as in Figures 4, 5, and 6, and discussed in Section 4.3.

We exclude any fits performed using fewer than 50 data points (the 20 km s^{-1} cloud, Cloud b, the Stone cloud, and Cloud c) or with fits determined to be poor upon visual inspection (SgrB. Main, Sgr C, Brick plus, and Cloud d). The Stone cloud, cloud b, and cloud c simply did not contain enough data for a meaningful fit. In the case of the 20 km s^{-1} cloud, the highest column density points show a slightly steeper power law than the rest of the region, which flagged a truncation at a very high x_{\min} , with a power-law fit of fewer than 50 data points and clearly not representative of the majority of the region. We also exclude the fits of four regions (SgrB. Main, Sgr C, Brick plus, and Cloud d)

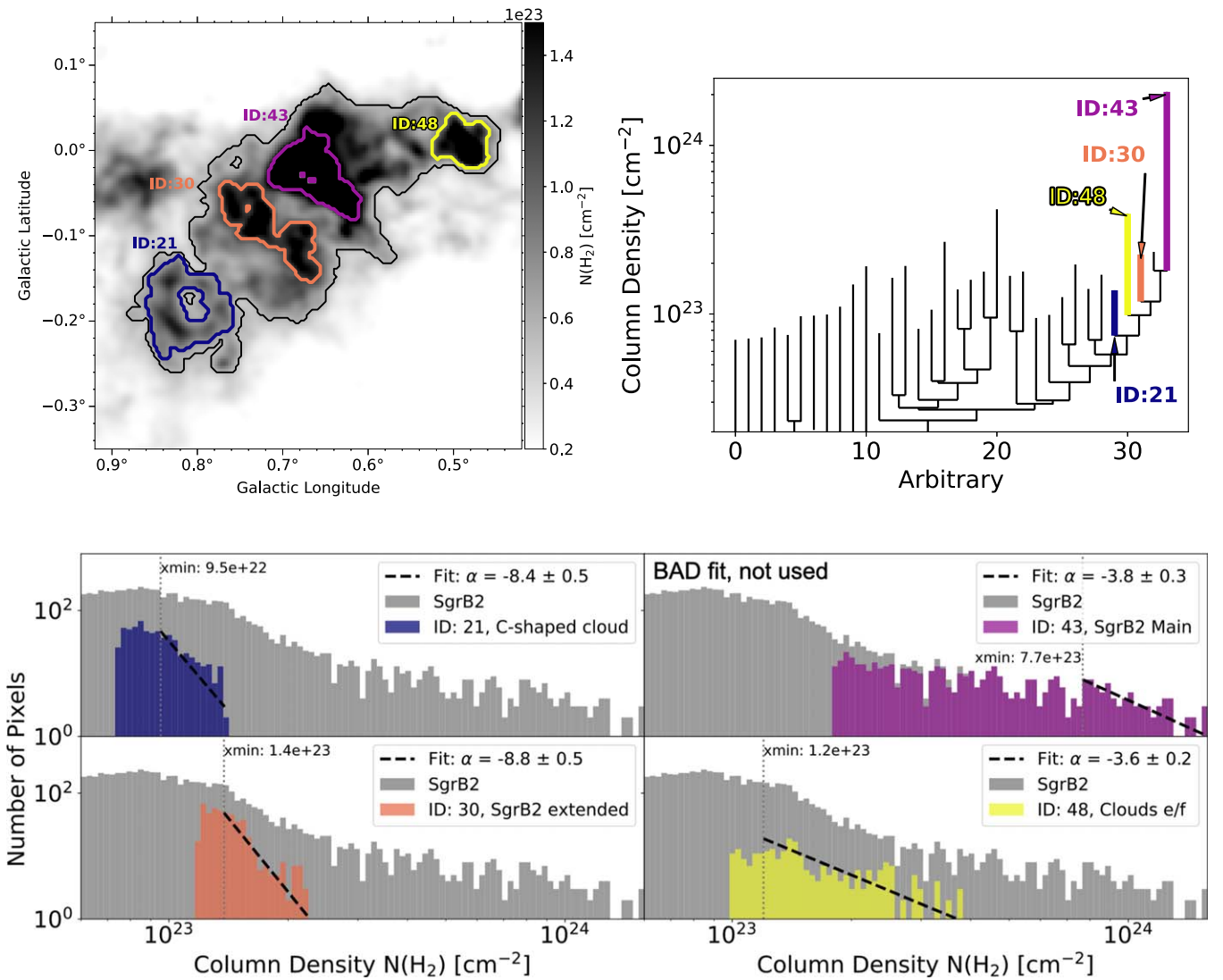


Figure 4. The SgrB. Main region comprises the highest column density gas in the CMZ. This figure highlights the extended SgrB2 region (black contour, same as the cyan contour in Figure 3) and four selected dendrogram structures within this region, color-coded and labeled in each plot: ID: 21 the “M0.8-0.2 ring” (M. Nonhebel et al. 2024), ID: 43 SgrB. Main, ID: 30 SgrB2 extended, and ID: 48 Clouds e/f. Each dendrogram structure is highlighted as a contour in the image in the top left, as well as within the larger dendrogram structure tree in the top right in the same color. The bottom images show the column density histogram of the entire SgrB2 region (from Figure 3) in gray and the column density PDF of each selected structure in the same color in which the structure is highlighted in the upper panels. Power-law fits to the individual dendrogram structures are shown as a dashed black line, with the automatically calculated x_{\min} value marked with a vertical dotted gray line and the fit slope given in the legend. Fits to the overall region and individual dendrogram structures are also presented in Table 4 and discussed in Section 4.3. The fit to ID: 43, SgrB2 main was determined not to be representative of the power-law slope of the full region, so was excluded from further analysis (discussed in more detail in Section 4.3).

that upon visual inspection do not appear to be high-quality fits to the full N-PDF above the x_{\min} value. For SgrB. Main, the x_{\min} value is $7.7 \times 10^{23} \text{ cm}^{-2}$ and well above the majority of the pixels in the region, making it not representative of the full region. For Sgr C and Brick plus, the algorithm seemed to miss a clear truncation from a steep to more shallow power-law slope. Finally, for Cloud d, the number of data points about x_{\min} is small, and the fit simply does not seem to uniquely represent the population.

4. Discussion

4.1. Comparison of Size, Linewidth, and Surface Density with Other Regions

In Figure 7 we compare the sizes, line widths ($\frac{\sigma^2}{R}$), and gas surface densities (Σ) of CMZ structures identified in this work

(in boldly outlined cyan) with Milky Way clouds from M. Heyer et al. (2009; in red), molecular clouds in NGC 300 from C. M. Faesi et al. (2018; in dark blue), and a sample of molecular clouds toward 10 of the nearest galaxies in the PHANGS-ALMA survey (E. Rosolowsky et al. 2021). The PHANGS-ALMA preliminary catalog from E. Rosolowsky et al. (2021) has a common 90 pc resolution; C. M. Faesi et al. (2018) achieves a spatial resolution of 10 pc; and M. Heyer et al.’s (2009) resolution ranges from about 0.3–3.0 pc at different molecular cloud distances. Our observations have a resolution of 1.5 pc, and the largest structures in the catalog are about 120 pc in size. Together, these data sample both galaxy disks and centers with physical scales that overlap. Our Milky Way CMZ probes higher surface densities than other samples for two reasons: (1) the surface density in the CMZ is higher than the Galactic disk, (2) compared with extragalactic CMZ’s from E. Rosolowsky et al. (2021), we have a higher physical

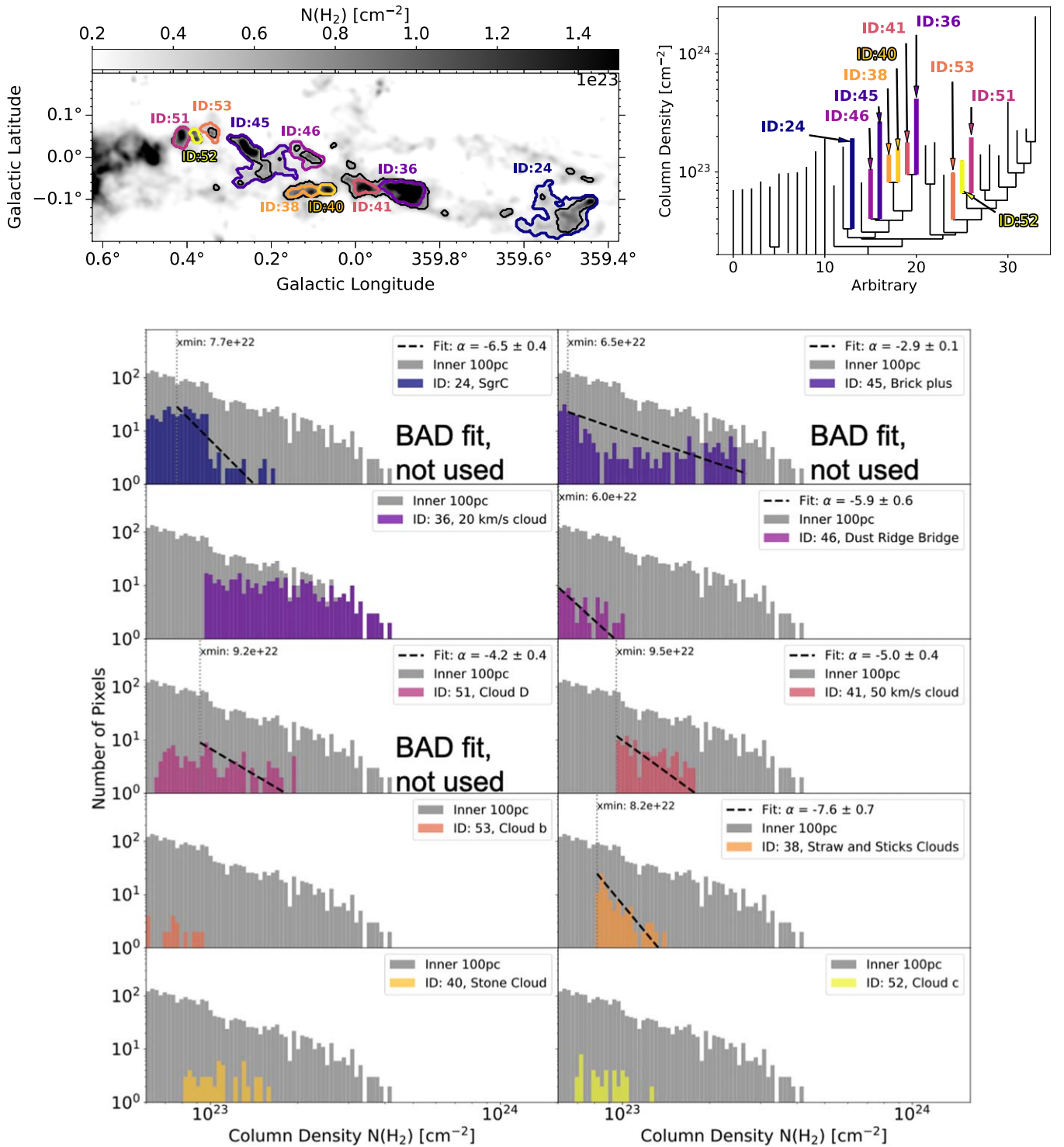


Figure 5. The inner 100 pc region is not well captured by a single column density contour, and is characterized by a series of high-column density clouds scattered about the CMZ. This figure is the same as Figure 4 except for structures in the inner 100 pc. The inner 100 pc region is shown with a black contour in the top-left image as defined in Figure 3 and 10 individual dendrogram structures within this region, which are color-coded and labeled in each plot: ID: 24 SgrC, ID: 45 Brick plus extended, ID: 36 the 20 km s^{-1} cloud, ID: 46 the dust ridge bridge, ID: 51 cloud D, ID: 41 the 50 km s^{-1} cloud, ID: 53 cloud b, ID: 38 the straw and sticks clouds, ID: 40 the stone cloud, and ID: 52 cloud c. Fits that utilized fewer than 50 data points (structures 36, 53, 40, and 52) were excluded, and the fits to structures 24, 45, and 51 were determined not to be representative of the power-law slope of the full region, so were excluded from further analysis (discussed in more detail in Section 4.3).

resolution and therefore, when observing dense gas, can probe higher average densities.

Figure 7 is inspired by an investigation into the effects of external pressure on virial equilibrium from G. B. Field et al.

(2011). We use Equation (8) from G. B. Field et al. (2011) to plot the solutions of pressure-bounded virial equilibrium for given external pressures in Figure 7 from $P_e/k = 10^5 \text{ K cm}^{-3}$ to $P_e/k = 10^9 \text{ K cm}^{-3}$, the same equation as used in other

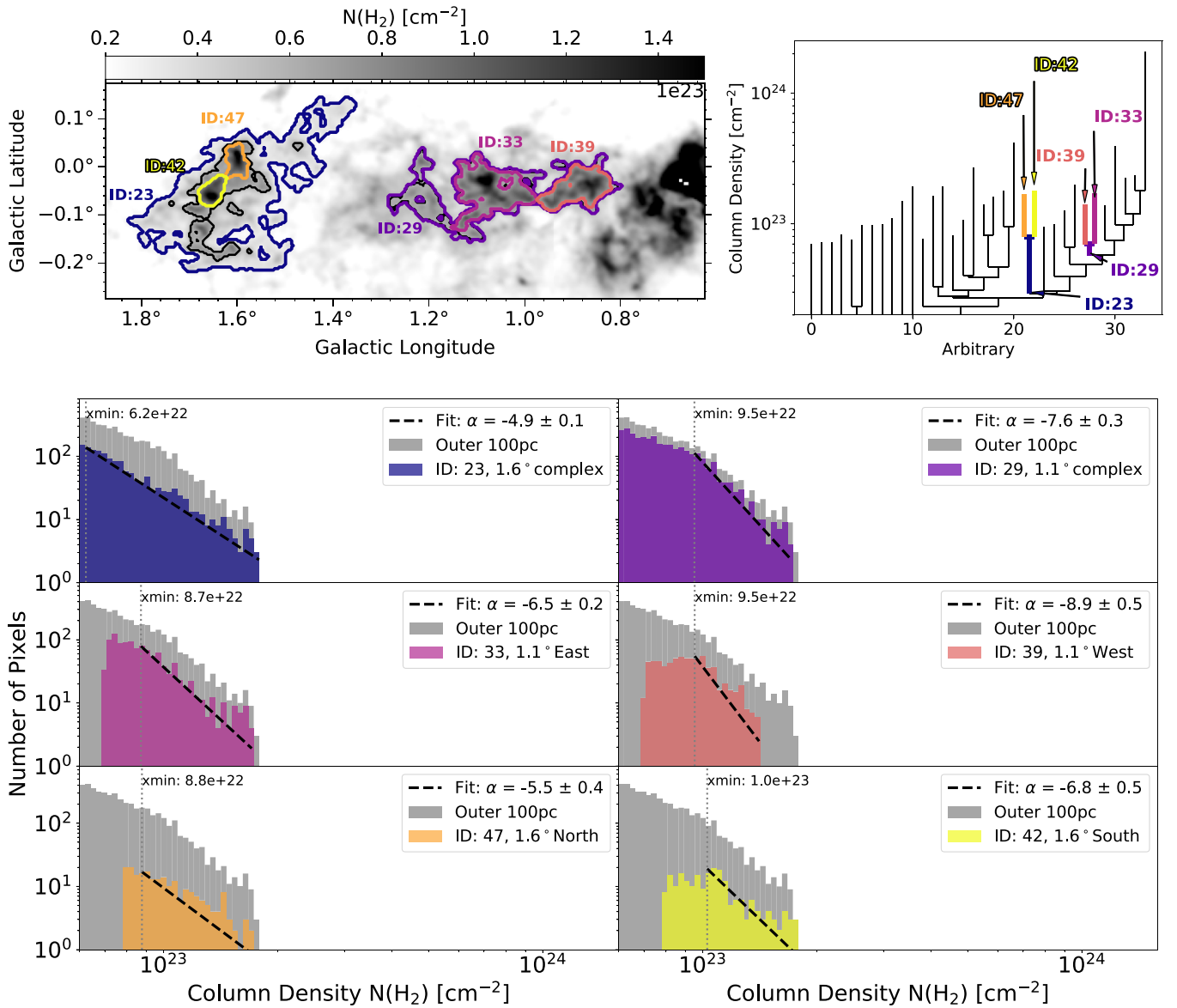


Figure 6. The outer 100 pc region contains two main complexes of clouds, the 1.6° and 1.1° complexes. This figure is the same as Figure 4 except for structures in the outer 100 pc. This figure highlights the outer 100 pc region with a black contour as defined in Figure 3 and six individual dendrogram structures within this region, which are color-coded and labeled in each plot: ID: 23 the 1.6° complex, ID: 29 the 1.1° complex, ID: 33 the 1.1° East cloud, ID: 39 the 1.1° West cloud, ID: 47 the 1.6° North cloud, and ID: 42 the 1.6° South cloud. The PDFs and power-law fits are discussed in more detail in Section 4.3.

recent works (e.g., D. L. Walker et al. 2018; N. Krieger et al. 2020; D. Callanan et al. 2023), see also P. C. Myers et al. (2022):

$$\frac{\sigma^2}{R} = \frac{1}{3} \left(\pi \Gamma G \Sigma + \frac{4P_e}{\Sigma} \right) \quad (5)$$

where Γ is assumed to be 0.73 (see G. B. Field et al. 2011). Of the 56 CMZ structures in Table 1, 11 do not have linewidth measurements from the MOPRA data (see Section 3.3) and are therefore excluded (IDs 0–7, 10, 55, and 56).

In general, the CMZ shows larger $\frac{\sigma^2}{R}$ and Σ values than Galactic disk measurements from M. Heyer et al. (2009) in the Milky Way or C. M. Faesi et al. (2018) in NGC 300. Our measurements probe higher densities than the sample from E. Rosolowsky et al. (2021) that also includes galaxy centers because our higher physical resolution (1.5 pc versus 90 pc)

means that our selected structures are focused on gas of higher average density, but we agree with their conclusion that galaxy centers are on average higher than galaxy disks (and farther from virial equilibrium) in this plot. CMZ structures are farther above the dashed gray line, which shows simple virial equilibrium in the absence of external pressure. Several authors argue that the majority of gas in the CMZ is unbound (e.g., X. Lu et al. 2019a; P. C. Myers et al. 2022; D. Callanan et al. 2023). N. Krieger et al. (2020) performed a detailed apples-to-apples comparison the CMZ with the center of NGC 253 and found that many structures in the CMZ on scales of ~ 10 –100 pc scales follow the expectations for gravitationally bound objects with virial parameters of about 2–3, while others have high virial parameters. Figure 7 shows that CMZ structures from this work are largely inconsistent with simple virial equilibrium, but could be considered to be in pressure-bounded virial equilibrium if in the presence of external

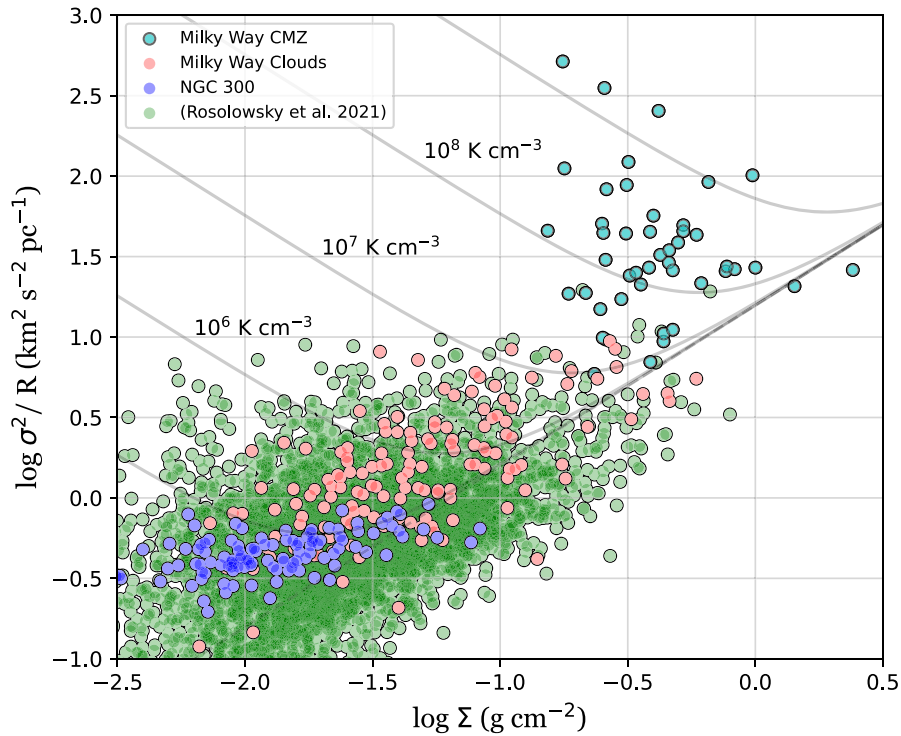


Figure 7. Structures in the CMZ (boldly outlined cyan points) have large line widths, but they may be consistent with virial equilibrium in the presence of high external pressures ($P_e/k > 10^7 \text{ K cm}^{-3}$). Plotted here are velocity dispersions (σ) squared divided by the structure’s effective radius vs. the surface density of gas for each structure (Σ_{gas}). The cyan shows structures in the CMZ with data from Tables 1 and 2. In red are values for Milky Way clouds from M. Heyer et al. (2009), in dark blue are clouds within NGC 300 from C. M. Faesi et al. (2018), and in green are clouds from the 10 most nearby galaxies with PHANGS-ALMA from E. Rosolowsky et al. (2021). See discussion in Section 4.1. Lines of virial equilibrium at constant external pressure are displayed as solid gray lines, using Equation (8) from G. B. Field et al. (2011) starting with $P_e = 10^5 \text{ K cm}^{-3}$ and going up to $P_e = 10^9 \text{ K cm}^{-3}$. The dashed gray line represents simple virial equilibrium with no external pressure. Points below a gray curve would be in virial equilibrium assuming the external pressure of the plotted curve. This figure is inspired by G. B. Field et al. (2011), D. L. Walker et al. (2018), and N. Krieger et al. (2020), and it highlights the complications of determining virial equilibrium in the presence of external pressure.

pressures exceeding $P_e/k > 10^{7-9} \text{ K cm}^{-3}$. As noted previously, our line widths are from a simple moment analysis, as in M. Heyer et al. (2009), C. M. Faesi et al. (2018), and E. Rosolowsky et al. (2021). However, multiple structures along the line of sight complicate the interpretation, and we refer the reader to Paper III for details on the kinematics of clouds within our catalog as well as R. Shetty et al. (2012), J. Kauffmann et al. (2017a), and J. D. Henshaw et al. (2016a) for detailed kinematics of the CMZ overall.

Figure 7 demonstrates that structures in the CMZ are either largely unbound or require a high external pressure ($P_e/k \sim 10^{7-9} \text{ K cm}^{-3}$) to be considered in pressure-bounded virial equilibrium, much higher than clouds in NGC 300 or throughout the rest of the Milky Way. This high external pressure is consistent with large-scale turbulent pressure estimates in this environment (e.g., J. M. D. Kruijssen & S. N. Longmore 2013; J. M. Rathborne et al. 2014; D. L. Walker et al. 2018).

As we have the full hierarchy of the structures from our analysis, we can assess whether the pressure within a parent structure is sufficient to confine the embedded leaf structure. Under the naïve assumption that the internal pressure of a branch structure is equivalent to the pressure exerted upon the leaf, we estimate the total external pressure as the sum of the turbulent, gravitational, and thermal pressures using

$$P_{\text{turb}} = \frac{1}{3} \rho \sigma^2 \quad (6)$$

$$P_{\text{grav}} = \frac{3}{4\pi} \frac{GM^2}{R^4} \quad (7)$$

$$P_{\text{therm}} = nk_B T \quad (8)$$

where all observed quantities (except for temperature) are the same as those reported in Tables 1 and 2. For the gas temperature, we assume a single value of 50 K in all cases. While this is a significant oversimplification, it is in line with the CMZ average of 50–200 K, or ~ 50 K in the densest regions (e.g., A. Ginsburg et al. 2016; N. Krieger et al. 2017). Moreover, this thermal pressure is orders of magnitude lower than the turbulent and gravitational pressures, and so any change in the temperature assumption has a negligible impact on the total pressure. We assume isotropic turbulence and a sphere of uniform density when calculating the turbulent and gravitational pressures. While these assumptions are highly simplistic, a detailed study is beyond the scope of this work, and these results serve as a rough estimate of the internal pressures, and whether or not they are of the same order of magnitude as that required for pressure-bounded virial equilibrium.

We then estimate the total pressure in each parent branch structure as $P_{\text{tot}} = (P_{\text{turb}} + P_{\text{grav}} + P_{\text{therm}})$, and compare this to the external pressure required to confine the leaf within, which is estimated by rearranging Equation (5) for P_e . The P_e values for each leaf and the P_{tot} of the corresponding parent branch are given in Table 3, along with the ratio of P_{tot}/P_e , where values

>1 indicate pressure confinement. Overall, we find that the majority of the leaves are consistent with being pressure-confined by their parent branch, and almost all are consistent within a factor of ~ 2 . While there are significant caveats related to the assumptions in this analysis, the results illustrate that the pressures involved are broadly sufficient to confine the structures.

Another possible source of pressure comes from the large-scale hot gas (e.g., L. Blitz et al. 1993). For example, T. Oka et al. (2019) argued for a large filling fraction of warm, low-density gas, which could provide the required pressure. We would need to invoke hot ($T > 10^6$ K) gas in order to produce this pressure thermally, if we assume that the required density is lower than or comparable to that of our molecular clouds. Understanding the magnitude, nature, and origin of pressure in the CMZ is critical for understanding how clouds in the CMZ become bound and form stars. J. Kauffmann et al. (2017a) uncovered an unusually steep size–linewidth relationship in the CMZ and found that on small scales the velocity dispersion goes down.

4.2. Comparison of Global SFRs with Other Regions

In Figure 8 we compare the SFRs and physical properties of CMZ structures derived in this work with other regions in the literature, from Milky Way clouds to high-redshift galaxies. These plots are largely built on the review paper from J. D. Henshaw et al. (2023) and pull data and relations from M. R. Krumholz (2014), M. J. Jiménez-Donaire et al. (2019), R. C. Kennicutt (1998), F. Bigiel et al. (2008), C. J. Lada et al. (2012), M. Querejeta et al. (2019), X.-J. Jiang et al. (2020), I. Bešlić et al. (2021), and references therein. In both plots, the cyan points are CMZ structures from this work (circles are molecular-cloud-sized leaves and crosses are large-scale branches), with data from Tables 1 and 3. The boldly outlined cyan points are overall CMZ points from J. D. Henshaw et al. (2023).

The methods for estimating both SFR and gas mass vary between and within the samples presented. Without doubt, some of the scatter observed in these plots could be attributed to the intrinsic uncertainty in any particular method for estimating these quantities. We do not presently have well-established SFR calibrations on molecular cloud-scale structures (leaves). In Section 3.5, we argue that our approach for cloud-scale SFRs is a reasonable first attempt and is based on freefall timescales of about 0.1–0.8 Myr (Table 3) and is consistent with expectations for high-mass star formation (e.g., C. Battersby et al. 2017). Our CMZ leaf points align with the global SFR relationships with no particular tuning on our part, just SFR estimates derived from first astrophysical principles. However, these cloud-scale (leaf) SFRs are still uncertain, and more detailed future work calibrating SFRs on cloud scales would be highly valuable.

To estimate the global uncertainties in this plot, we can refer to our own CMZ, where the scatter in the SFR measurements depending on technique account for about a factor of 2 of the variation observed (A. T. Barnes et al. 2017). Without a more detailed apples-to-apples comparison of measurement techniques in these samples, we cannot be sure how much of the scatter or trends may be due to variation in measurement techniques, however, if the global CMZ SFR measurement is to be any guide, the measurement variation of about a factor of 2 is much less than the observed scatter of more than 1 dex.

In the left plot, we compare the SFR surface density (Σ_{SFR}) with the gas surface density (Σ_{gas}). J. D. Henshaw et al. (2023) compared the CMZ data point overall (cyan with bold outline, with three possible positions in this plot depending on geometrical assumption—circles assume face-on disk geometry, triangles indicate a face-on ring geometry, and squares indicate an edge-on geometry) and found that the CMZ overall is roughly consistent, or marginally inconsistent depending on geometry, with the R. C. Kennicutt (1998) relationship. J. M. D. Kruijssen et al. (2014) reported that the CMZ overall is consistent with the F. Bigiel et al. (2008) relationship, which would support the hypothesis that some mechanism is inhibiting star formation in the CMZ.

We find considerable scatter in the large sample of CMZ structures compiled in this work, however, the majority of the points lie above the R. C. Kennicutt (1998) relationship and closely follow comparable regions from the Milky Way, starburst, and high-redshift galaxies. CMZ data points associated with leaves (circles in Figure 8) tend to represent molecular cloud sized structures and follow this trend most closely. CMZ data points associated with branches (crosses in Figure 8) are more representative of the CMZ overall, including gas not associated with individual molecular clouds, and lie between the R. C. Kennicutt (1998) and F. Bigiel et al. (2008) relationships, in close agreement with the CMZ overall data points from J. D. Henshaw et al. (2023).

The right plot of Figure 8 compares the various regions’ SFRs with their dense gas mass. As discussed in detail in J. D. Henshaw et al. (2023), the CMZ overall (boldly outlined cyan circle) is clearly inconsistent with this so-called dense gas–star formation relationship (see, e.g., S. N. Longmore et al. 2013a), first proposed by Y. Gao & P. M. Solomon (2004) and extended by C. J. Lada et al. (2010, 2012). However, our new detailed analysis finds that while branches (crosses in Figure 8) similarly show a significant deviation from the dense gas–star formation relation, leaves (circles in Figure 8 representing individual molecular clouds) match these global dense gas–star formation relations quite well, with a similar scatter as other regions.

The finding that molecular-cloud-sized structures in the CMZ (leaves, cyan circles in Figure 8) seem to match the global SFR versus dense gas relationship is significant. Several previous works have found a significant lack of substructure across the CMZ on ~ 0.1 pc scales (X. Lu et al. 2019a, 2019b; C. Battersby et al. 2020; H. P. Hatchfield et al. 2020). The emerging paradigm seems to be that CMZ gas, which is engaged in the star formation process (such as that contained within individual molecular clouds), forms stars as normal. However, much of the CMZ’s dense gas (the CMZ overall data points) is simply not engaged in the star formation process.

4.3. N-PDFs Power-law fits

In general, observations of quiescent molecular clouds have N-PDFs that are consistent with a lognormal distribution, indicating that they are dominated by turbulence. Some work (e.g., J. Alves et al. 2017), however, suggests that molecular cloud N-PDFs are consistent with steep power-law slopes. It is agreed that molecular clouds with signatures of star formation show a shallower power-law tail at high densities, indicating the presence of self-gravity in addition to the turbulent lognormal (or steep power-law) component that dominates at lower densities. These works demonstrate that more prolific

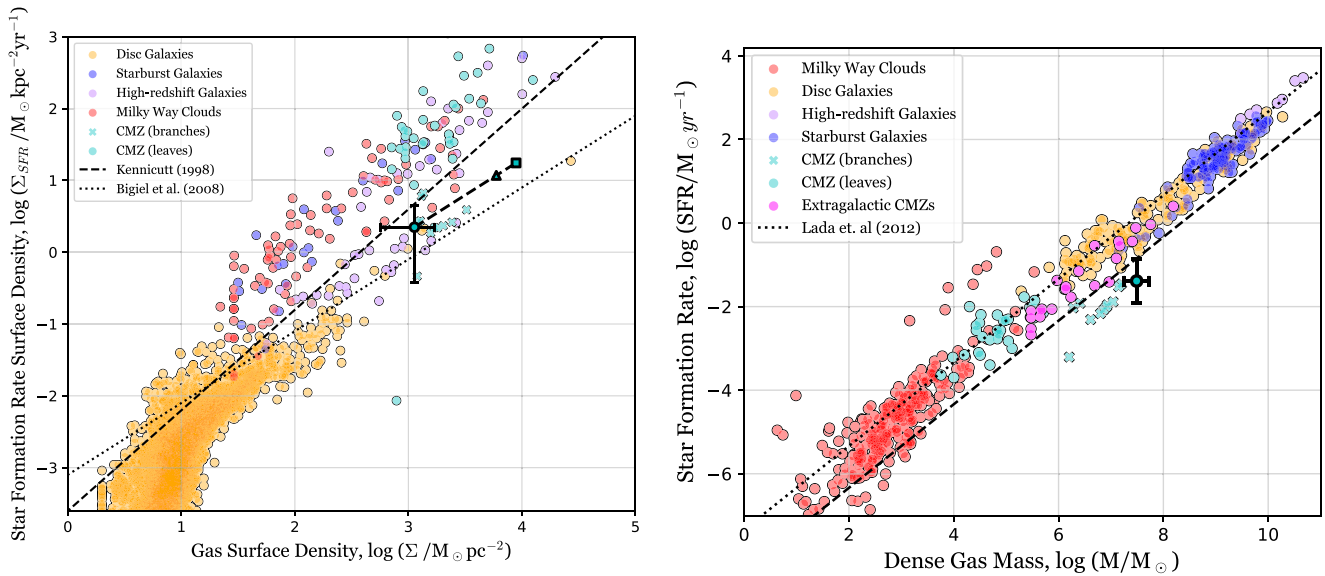


Figure 8. We compare the SFR vs. density properties of CMZ structures identified in this work (cyan) with structures in the literature, from Milky Way clouds to high-redshift galaxies. While the CMZ overall (bold cyan circle) falls an order of magnitude below the dense gas–star formation relation, the individual clouds in the CMZ show better agreement. In both plots, the cyan points are CMZ structures identified in this work (circles are molecular-cloud-sized leaves and crosses are larger branches) with values from Tables 1 and 3, while the boldly outlined cyan shapes (circle, triangle, and square) are the CMZ overall from J. D. Henshaw et al. (2023; each assuming a different CMZ geometry in the density calculation; see Section 3.1.3 in J. D. Henshaw et al. 2023, for details). The gray-outlined colored points are from the literature (see M. R. Krumholz 2014; M. J. Jiménez-Donaire et al. 2019; J. D. Henshaw et al. 2023, and references therein) Left panel: the SFR surface density (Σ_{SFR}) is plotted as a function of the gas surface density (Σ_{gas}) with the scaling relations from R. C. Kennicutt (1998) and F. Bigiel et al. (2008) (power-law slopes of $n = 1.4$ and $n = 1.0$, respectively) plotted on top. Right panel: the SFR vs. mass of dense gas (M_{dense}) with the scaling relation from C. J. Lada et al. (2012) shown as a dotted line and a factor of 10 below this relation shown as a dashed line. (The out-lying low cyan point on the left plot is G357.070-0.770 (Structure ID: 1), which is an isolated structure, far off the Galactic plane ($b = -0.770$), and is likely not in the CMZ.)

star formation is correlated with a shallower power-law tail (J. Kainulainen et al. 2009; D. Russeil et al. 2013; J. Abreu-Vicente et al. 2015; A. M. Stutz & J. Kainulainen 2015; N. Schneider et al. 2022). Both D. Russeil et al. (2013) and A. M. Stutz & J. Kainulainen (2015) analyzed the N-PDFs of subregions within a high-mass star-forming region (NGC 6334 and Orion, respectively) using Herschel data. D. Russeil et al. (2013) found the shallowest power-law slope in the central star-forming region ($p = -1.48$) with steeper slopes in the less-evolved regions (from $p = -3.14$ to $p = -5.58$). A. M. Stutz & J. Kainulainen (2015) found that the regions with the highest Class 0 fractions have the shallowest slopes (down to $p = -0.9$) and the regions with the lowest Class 0 fraction have the steepest slopes (up to $p = -2.95$). W. Lim et al. (2016) studied the N-PDF of an extreme Infrared Dark Cloud and found that it is consistent with a lognormal, with some tentative evidence for a deviation to a power law at high densities. They found similar results using both a near-IR + mid-IR dust extinction technique and a Herschel Far-IR dust emission, and reported the Herschel Galactic Gaussian method (introduced in C. Battersby et al. 2011, and used in this work) to be well suited for the subtraction of the large-scale Galactic fore/background. J. Abreu-Vicente et al. (2015) performed the most comprehensive study of molecular cloud N-PDFs to date, studying hundreds of molecular clouds across 3 orders of magnitude in mass and spanning the evolutionary sequence from starless, to star-forming, to HII regions using ATLASGAL data. They found that starless regions have N-PDFs consistent with a lognormal distribution, while star-forming regions show a mix of lognormal at low densities and a power-law tail at high densities, with an integrated average power-law slope of $p = -3.8$. The HII region population is dominated by a

shallower power law, with an integrated average slope of $p = -2.1$. Similar results are reported by N. Schneider et al. (2022). Work by H. H.-H. Chen et al. (2018) studies the anatomy of N-PDFs using dendrograms on both observations and simulations, and they found that individual substructures have power-law indices that are different from the N-PDF of the entire region, which may indicate different stages of gravitational collapse.

The slopes of our N-PDFs are generally quite steep compared with literature values (typically $-6 < \alpha < -1$) and range from $\alpha = -2.5$ at the shallowest (SgrB2 overall region) to $\alpha = -8.9$ (the 1.1 West cloud, ID: 39) at the steepest, as shown in Figure 9. A steep power law can indicate non-star-forming turbulent gas, which could also have been fit with a lognormal. If these regions reflect the turbulent, chaotic gas rather than star-forming gas, then a steep power-law slope is not surprising. Finding strong turbulence even at these high densities is not surprising in this part of the Galaxy (e.g., R. Shetty et al. 2012; J. D. Henshaw et al. 2016b, 2023; A. Ginsburg et al. 2016).

We present the power-law slopes in Table 4. These are plotted against the best SFR estimate (from Table 3) in Figure 9. After all of the PDF exclusions based on quality of fit (see Section 3.6) and one missing SFR (ID: 29, region was a branch but was too small for the IR-based SFR method, see Section 3.5 for details), we are left with 11 data points.

As described earlier in this section, typically, a shallower power-law tail is thought to be associated with more vigorous star formation. We see this trend in our overall region fits. The Sgr B2 region is considered one of the most actively star-forming regions in the Galaxy and has the shallowest power law overall ($\alpha = -2.5 \pm 0.1$), the outer 100 pc overall region is largely considered non-star-forming and has the steepest power

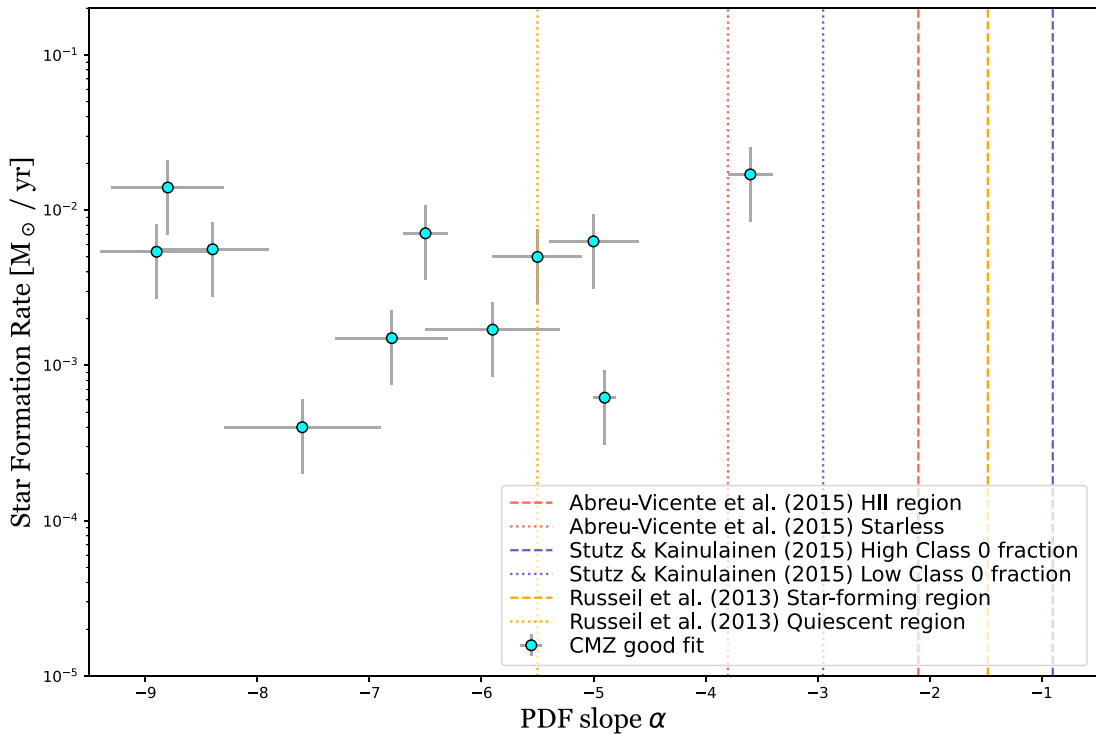


Figure 9. A comparison of the N-PDF slope of CMZ structures (in cyan) with their SFR shows, at best, a marginal trend of steeper N-PDF slope with decreasing SFR, but with very small significance and a number of suspicious outliers. We plot here the PDF slope α and their errors from Table 4 (described in further detail in Section 3.6) on the x-axis vs. the SFRs from Table 3 (discussed in Section 3.5) assuming an error of 50% for each point. As described in Section 4.3, some regions appear to be in good agreement with the overall literature trend of a steeper N-PDF slope indicating a lower SFR, while other regions buck this trend. We plot various literature N-PDF slopes as vertical lines, with dashed lines indicating the more actively star-forming average slopes and dotted lines the more quiescent slopes from these publications. This plot also demonstrates that our slopes tend to be steeper than most reported literature values.

law overall ($\alpha = -7.3 \pm 0.2$), while the inner 100 pc overall region is in the middle ($\alpha = -3.3 \pm 0.1$). However, the results are not uniformly in agreement on the individual cloud scale. Figure 9 shows a correlation in the majority of the regions (7 of the 11) with three outliers significantly above, and one outlier significantly below this trend in their SFR. The three high outliers are 1.1 west (ID: 39), the bubble (ID: 21) (M. Nonhebel et al. 2024), and SgrB2 extended (ID: 30), and the one low outlier is the 1.6 complex (ID: 23).

Column density maps only tell us part of the story of the CMZ, but N-PDF slopes allow us to connect this extreme region of the Galaxy with our solar neighborhood, simulations, and other regions. The conclusion that the PDF slope in the CMZ is generally steeper than others reported in the literature may be due to the fact that many of our structures sample large physical areas, with a high fraction of dense gas that is not involved in the star formation process (C. Battersby et al. 2020). We note that the majority of the PDFs are complex and may not be well described by a single power law (compare with the multiple power laws reported by N. Schneider et al. 2015, 2022). We have selectively chosen a handful (11) of regions, plus the three overall CMZ regions, that appear to be well fit by this metric for our analysis and to be able to compare with other regions.

5. Conclusions

The CMZ is the hub at the center of the Milky Way Galaxy that connects gas flowing from Galactic scales with the central nucleus. We present a hierarchical structure catalog of the CMZ and measurements of the physical and kinematic properties, as

well as SFR estimates of each structure. We compare the properties derived with other regions in the Milky Way and external galaxies. As part of this work, we release the full dendrogram hierarchical structure and the full catalog in the form of a machine-readable table that includes all of the columns from Tables 1–4 in one coherent framework. Below, we summarize key conclusions drawn from this work:

1. Using the column density map from Paper I (C. Battersby et al. 2025), we develop a multiscale catalog of dense gas structures in the CMZ using ASTRODENDRO. We identify 11 levels of hierarchical structure, with a total of 57 branches and leaves, with structures on the scale of the entire CMZ down to individual molecular clouds.
2. We compute and report the physical properties of each structure in our dendrogram hierarchy. Using Herschel data products from Paper I, we report the area, central coordinates, column densities, dust temperatures, masses, radii, and freefall times of each structure.
3. We calculate kinematic properties of each structure using integrated spectra toward each structure with the P. A. Jones et al. (2012) MOPRA 3mm data. We compute the kinematic properties using simple moment analysis in three molecular line transitions: HNCO 4(0, 4)–3(0, 3), HCN 1–0 ($F=2-1$), and HC₃N 10–9.
4. We integrate the Paper I modified blackbody fits to compute the “cool” far-IR luminosity of each structure (incorporating wavelengths from 160 to 500 μ m) and combine with a “warm” luminosity estimate (adding in

wavelengths 5.8–24 μm from Spitzer) from A. T. Barnes et al. (2017) to derive a total IR luminosity for each structure.

5. For the branches in our hierarchical tree with a total area greater than 1000 pc^2 , we use the R. C. Kennicutt (1998) scaling relationship, to convert total IR luminosities to SFR estimates.
6. For leaves in our catalog, which mostly represent individual molecular clouds, we use two methods to estimate SFRs. Where available, we use the SFRs from H. P. Hatchfield et al. (2024) using the CMZoom survey (C. Battersby et al. 2020). In the remainder of leaves, we develop a new “freefall” SFR estimation method based on the work from A. T. Barnes et al. (2017), which uses the total luminosity of a structure to infer the embedded stellar mass, then the freefall time as the timescale for star formation. This method agrees well with the H. P. Hatchfield et al. (2024) SFRs in overlapping regions.
7. We compare our structure sizes, line widths, and gas surface densities with other molecular clouds in the Milky Way (M. Heyer et al. 2009), NGC 300 (C. M. Faesi et al. 2018), and the 10 most nearby PHANGS-ALMA galaxies from E. Rosolowsky et al. (2021). Similar to previous work, we find that structures in the CMZ are either gravitationally unbound or could be consistent with virial equilibrium if they are in the presence of a high external pressure ($P_e/k > 10^{7-9} \text{ K cm}^{-3}$). Using simplistic physical assumptions, we estimate the external pressure for each leaf in our catalog, based on the thermal, turbulent, and gravitational pressure of its surrounding parent branch. We find that the majority of our leaves are consistent with being in pressure-bounded equilibrium.
8. We place the gas densities and SFRs of our CMZ structures in the context of a variety of systems, from Milky Way clouds to high-redshift galaxies, by comparing their positions on standard SFR versus gas surface density and dense gas mass plots. It has already been reported (e.g., K. Immer et al. 2012; S. N. Longmore et al. 2012; J. D. Henshaw et al. 2023) that the CMZ overall is in modest agreement with the Schmidt–Kennicutt star formation relation and falls well below the Gao–Solomon dense gas–star formation relation. However, we find that individual molecular-cloud-sized CMZ structures align well with other Milky Way and extragalactic regions and are in agreement with these star formation relationships.
9. Finally, we perform simple power-law fits to the N-PDF of three main CMZ overall regions (defined by natural boundaries in the column density map to be the Outer 100 pc region, Sgr B2 extended, and the Inner 100 pc region) as well as to a handful of structures in the catalog. We find that our power-law slopes are steeper than those in the literature ($-9 < \alpha < -2$ in this work compared with $-6 < \alpha < -1$ in the literature). Most of our regions hint at a general trend of steeper N-PDF slopes for lower SFR.

Acknowledgments

C.B. gratefully acknowledges funding from National Science Foundation (NSF) under award Nos. 1816715, 2108938,

2206510, and CAREER 2145689, as well as from the National Aeronautics and Space Administration through the Astrophysics Data Analysis Program under award “3-D MC: Mapping Circumnuclear Molecular Clouds from X-ray to Radio,” grant No. 80NSSC22K1125. D.W. and D.L. gratefully acknowledge funding from the NSF under award No. 1816715 and D.L. also acknowledges funding from the National Science Foundation under award Nos. 2108938, and CAREER 2145689, as well as from the NASA Connecticut Space Grant Consortium under PTE Federal award No: 80NSSC20M0129. A.G. acknowledges funding from NSF awards AST 2008101 and 2206511 and CAREER 2142300. J.D.H. gratefully acknowledges financial support from the Royal Society (University Research Fellowship; URF/R1/221620). R.S.K. and S.C.O.G. acknowledge financial support from the European Research Council via the ERC Synergy Grant “ECOGAL” (project ID 855130), from the German Excellence Strategy via the Heidelberg Cluster of Excellence (EXC 2181—390900948) “STRUCTURES,” and from the German Ministry for Economic Affairs and Climate Action in project “MAINN” (funding ID 500O2206). E.A.C.M. gratefully acknowledges funding from the National Science Foundation under award Nos. 1813765, 2115428, 2206509, and CAREER 2339670. M.C.S. acknowledges financial support from the European Research Council under the ERC Starting Grant “GalFlow” (grant 101116226). Q.Z. acknowledges the support from the National Science Foundation under award No. 2206512. Herschel is an ESA space observatory with science instruments provided by European-led Principal Investigator consortia and with important participation from NASA. COOL Research DAO is a Decentralized Autonomous Organization supporting research in astrophysics aimed at uncovering our cosmic origins.

Software: This work made use of Astropy: (<http://www.astropy.org>) a community-developed core Python package and an ecosystem of tools and resources for astronomy (Astropy Collaboration et al. 2013, 2018, 2022). This research made use of astrodendro, a Python package to compute dendrograms of Astronomical data (<http://www.dendrograms.org/>) as well as SAO Image ds9 (W. A. Joye & E. Mandel 2003). This research made use of Montage. It is funded by the National Science Foundation under grant No. ACI-1440620, and was previously funded by the National Aeronautics and Space Administration’s Earth Science Technology Office, Computation Technologies Project, under Cooperative Agreement Number NCC5-626 between NASA and the California Institute of Technology. This research has made use of NASA’s Astrophysics Data System Bibliographic Services.

ORCID iDs

Cara Battersby  <https://orcid.org/0000-0002-6073-9320>
 Daniel L. Walker  <https://orcid.org/0000-0001-7330-8856>
 Ashley Barnes  <https://orcid.org/0000-0003-0410-4504>
 Adam Ginsburg  <https://orcid.org/0000-0001-6431-9633>
 Dani Lipman  <https://orcid.org/0000-0002-5776-9473>
 Danya Alboslani  <https://orcid.org/0009-0005-9578-2192>
 H Perry Hatchfield  <https://orcid.org/0000-0003-0946-4365>
 John Bally  <https://orcid.org/0000-0001-8135-6612>
 Simon C. O. Glover  <https://orcid.org/0000-0001-6708-1317>
 Jonathan D. Henshaw  <https://orcid.org/0000-0001-9656-7682>
 Katharina Immer  <https://orcid.org/0000-0003-4140-5138>
 Ralf S. Klessen  <https://orcid.org/0000-0002-0560-3172>
 Steven N. Longmore  <https://orcid.org/0000-0001-6353-0170>

Elisabeth A. C. Mills  <https://orcid.org/0000-0001-8782-1992>
 Sergio Molinari  <https://orcid.org/0000-0002-9826-7525>
 Rowan Smith  <https://orcid.org/0000-0002-0820-1814>
 Mattia C. Sormani  <https://orcid.org/0000-0001-6113-6241>
 Robin G. Tress  <https://orcid.org/0000-0002-9483-7164>
 Qizhou Zhang  <https://orcid.org/0000-0003-2384-6589>

References

- Abreu-Vicente, J., Kainulainen, J., Stutz, A., Henning, T., & Beuther, H. 2015, *A&A*, **581**, A74
- Alstott, J., Bullmore, E., & Plenz, D. 2014, *PLoS*, **9**, e85777
- Alves, J., Lombardi, M., & Lada, C. 2017, *A&A*, **606**, L2
- Astropy Collaboration, Price-Whelan, A. M., Lim, P. L., et al. 2022, *ApJ*, **935**, 167
- Astropy Collaboration, Price-Whelan, A. M., Sipőcz, B. M., et al. 2018, *AJ*, **156**, 123
- Astropy Collaboration, Robitaille, T. P., Tollerud, E. J., et al. 2013, *A&A*, **558**, A33
- Ballesteros-Paredes, J., Vázquez-Semadeni, E., Gazol, A., et al. 2011, *MNRAS*, **416**, 1436
- Bally, J., Stark, A. A., Wilson, R. W., & Henkel, C. 1987, *ApJS*, **65**, 13
- Barnes, A. T., Longmore, S. N., Battersby, C., et al. 2017, *MNRAS*, **469**, 2263
- Battersby, C., Bally, J., Ginsburg, A., et al. 2011, *A&A*, **535**, A128
- Battersby, C., Bally, J., & Svoboda, B. 2017, *ApJ*, **835**, 263
- Battersby, C., Keto, E., Walker, D., et al. 2020, *ApJS*, **249**, 35
- Battersby, C., Walker, D., Barnes, A., et al. 2024, Papers I & II (Battersby et al. 2024a, b), Harvard Dataverse, doi:10.7910/DVN/7DOJG5
- Battersby, C., Walker, D. L., Barnes, A., et al. 2025, *ApJ*, **984**, 156
- Benjamin, R. A., Churchwell, E., Babler, B. L., et al. 2003, *PASP*, **115**, 953
- Bešlić, I., Barnes, A. T., Bigiel, F., et al. 2021, *MNRAS*, **506**, 963
- Bigiel, F., Leroy, A., Walter, F., et al. 2008, *AJ*, **136**, 2846
- Blitz, L., Binney, J., Lo, K. Y., Bally, J., & Ho, P. T. P. 1993, *Natur*, **361**, 417
- Burkhart, B., Stalpes, K., & Collins, D. C. 2017, *ApJL*, **834**, L1
- Callanan, D., Longmore, S. N., Battersby, C., et al. 2023, *MNRAS*, **520**, 4760
- Carey, S. J., Noriega-Crespo, A., Mizuno, D. R., et al. 2009, *PASP*, **121**, 76
- Chen, H. H.-H., Burkhart, B., Goodman, A., & Collins, D. C. 2018, *ApJ*, **859**, 162
- Clark, P. C., Glover, S. C. O., Ragan, S. E., Shetty, R., & Klessen, R. S. 2013, *ApJL*, **768**, L34
- Clauset, A., Shalizi, C. R., & Newman, M. E. J. 2009, *SIAMR*, **51**, 661
- Clavel, M., Terrier, R., Goldwurm, A., et al. 2013, *A&A*, **558**, A32
- Crutcher, R. M., Roberts, D. A., Mehringer, D. M., & Troland, T. H. 1996, *ApJL*, **462**, L79
- Davies, B., Hoare, M. G., Lumsden, S. L., et al. 2011, *MNRAS*, **416**, 972
- Faesi, C. M., Lada, C. J., & Forbrich, J. 2018, *ApJ*, **857**, 19
- Federrath, C., Glover, S. C. O., Klessen, R. S., & Schmidt, W. 2008, *PhSt*, **132**, 014025
- Federrath, C., & Klessen, R. S. 2013, *ApJ*, **763**, 51
- Federrath, C., Rathborne, J. M., Longmore, S. N., et al. 2016, *ApJ*, **832**, 143
- Field, G. B., Blackman, E. G., & Keto, E. R. 2011, *MNRAS*, **416**, 710
- Gao, Y., & Solomon, P. M. 2004, *ApJ*, **606**, 271
- Ginsburg, A., Bally, J., Barnes, A., et al. 2018, *ApJ*, **853**, 171
- Ginsburg, A., Henkel, C., Ao, Y., et al. 2016, *A&A*, **586**, A50
- Girichidis, P., Konstandin, L., Whitworth, A. P., & Klessen, R. S. 2014, *ApJ*, **781**, 91
- Goicoechea, J. R., Rodríguez-Fernández, N. J., & Cernicharo, J. 2004, *ApJ*, **600**, 214
- Goodman, A. A., Rosolowsky, E. W., Borkin, M. A., et al. 2009, *Natur*, **457**, 63
- Goto, M., Indriolo, N., Geballe, T. R., & Usuda, T. 2013, *JPCA*, **117**, 9919
- Gravity Collaboration, Abuter, R., Amorim, A., et al. 2019, *A&A*, **625**, L10
- GRAVITY Collaboration, Abuter, R., Amorim, A., et al. 2021, *A&A*, **647**, A59
- Güsten, R., & Henkel, C. 1983, *A&A*, **125**, 136
- Harada, N., Riquelme, D., Viti, S., et al. 2015, *A&A*, **584**, A102
- Hatchfield, H. P., Battersby, C., Barnes, A. T., et al. 2024, *ApJ*, **962**, 14
- Hatchfield, H. P., Battersby, C., Keto, E., et al. 2020, *ApJS*, **251**, 14
- Hatchfield, H. P., Sormani, M. C., Tress, R. G., et al. 2021, *ApJ*, **922**, 79
- Hennebelle, P., & Falgarone, E. 2012, *A&ARv*, **20**, 55
- Henshaw, J. D., Barnes, A. T., Battersby, C., et al. 2023, in ASP Conf. Ser. 534, Protostars and Planets VII, ed. S. Inutsuka et al. (San Francisco, CA: ASP), **83**
- Henshaw, J. D., Longmore, S. N., & Kruijssen, J. M. D. 2016a, *MNRAS*, **463**, L122
- Henshaw, J. D., Longmore, S. N., Kruijssen, J. M. D., et al. 2016b, *MNRAS*, **457**, 2675
- Heyer, M., Krawczyk, C., Duval, J., & Jackson, J. M. 2009, *ApJ*, **699**, 1092
- Immer, K., Menten, K. M., Schuller, F., & Lis, D. C. 2012, *A&A*, **548**, A120
- Indriolo, N., Neufeld, D. A., Gerin, M., et al. 2015, *ApJ*, **800**, 40
- Jiang, X.-J., Greve, T. R., Gao, Y., et al. 2020, *MNRAS*, **494**, 1276
- Jiménez-Donaire, M. J., Bigiel, F., Leroy, A. K., et al. 2019, *ApJ*, **880**, 127
- Jones, P. A., Burton, M. G., Cunningham, M. R., et al. 2012, *MNRAS*, **419**, 2961
- Joye, W. A., & Mandel, E. 2003, in ASP Conf. Ser. 295, Astronomical Data Analysis Software and Systems XII, ed. H. E. Payne, R. I. Jedrzejewski, & R. N. Hook (San Francisco, CA: ASP), **489**
- Kainulainen, J., Beuther, H., Henning, T., & Plume, R. 2009, *A&A*, **508**, L35
- Kauffmann, J., Pillai, T., Zhang, Q., et al. 2017a, *A&A*, **603**, A89
- Kauffmann, J., Pillai, T., Zhang, Q., et al. 2017b, *A&A*, **603**, A90
- Kendrew, S., Ginsburg, A., Johnston, K., et al. 2013, *ApJL*, **775**, L50
- Kennicutt, R. C., Jr. 1998, *ARA&A*, **36**, 189
- Kennicutt, R. C., & Evans, N. J. 2012, *ARA&A*, **50**, 531
- Klaus, A., Yu, S., & Plenz, D. 2011, *PLoS*, **6**, e19779
- Klessen, R. S. 2000, *ApJ*, **535**, 869
- Koepferl, C. M., Robitaille, T. P., Morales, E. F. E., & Johnston, K. G. 2015, *ApJ*, **799**, 53
- Krieger, N., Bolatto, A. D., Koch, E. W., et al. 2020, *ApJ*, **899**, 158
- Krieger, N., Ott, J., Beuther, H., et al. 2017, *ApJ*, **850**, 77
- Kroupa, P. 2001, *MNRAS*, **322**, 231
- Kruijssen, J. M. D., Dale, J. E., Longmore, S. N., et al. 2019, *MNRAS*, **484**, 5734
- Kruijssen, J. M. D., & Longmore, S. N. 2013, *MNRAS*, **435**, 2598
- Kruijssen, J. M. D., Longmore, S. N., Elmegreen, B. G., et al. 2014, *MNRAS*, **440**, 3370
- Krumholz, M. R. 2014, *PhR*, **539**, 49
- Krumholz, M. R., Kruijssen, J. M. D., & Crocker, R. M. 2017, *MNRAS*, **466**, 1213
- Lada, C. J., Forbrich, J., Lombardi, M., & Alves, J. F. 2012, *ApJ*, **745**, 190
- Lada, C. J., Lombardi, M., & Alves, J. F. 2010, *ApJ*, **724**, 687
- Lim, W., Tan, J. C., Kainulainen, J., Ma, B., & Butler, M. J. 2016, *ApJL*, **829**, L19
- Lipman, D., Battersby, C., Walker, D. L., et al. 2025, *ApJ*, **984**, 159
- Lis, D. C., Serabyn, E., Zylka, R., & Li, Y. 2001, *ApJ*, **550**, 761
- Lombardi, M., Alves, J., & Lada, C. J. 2015, *A&A*, **576**, L1
- Longmore, S. N., Bally, J., Testi, L., et al. 2013a, *MNRAS*, **429**, 987
- Longmore, S. N., Kruijssen, J. M. D., Bally, J., et al. 2013b, *MNRAS*, **433**, L15
- Longmore, S. N., Rathborne, J., Bastian, N., et al. 2012, *ApJ*, **746**, 117
- Lu, X., Li, S., Ginsburg, A., et al. 2021, *ApJ*, **909**, 177
- Lu, X., Mills, E. A. C., Ginsburg, A., et al. 2019a, *ApJS*, **244**, 35
- Lu, X., Zhang, Q., Kauffmann, J., et al. 2017, *ApJ*, **839**, 1
- Lu, X., Zhang, Q., Kauffmann, J., et al. 2019b, *ApJ*, **872**, 171
- Meng, F., Sánchez-Monge, Á., Schilke, P., et al. 2022, *A&A*, **666**, A31
- Mills, E. A. C., Corby, J., Clements, A. R., et al. 2018, *ApJ*, **869**, 121
- Mills, E. A. C., & Morris, M. R. 2013, *ApJ*, **772**, 105
- Molinari, S., Bally, J., Noriega-Crespo, A., et al. 2011, *ApJL*, **735**, L33
- Molinari, S., Schisano, E., Elia, D., et al. 2016, *A&A*, **591**, A149
- Morris, M., & Serabyn, E. 1996, *ARA&A*, **34**, 645
- Mould, J. R. 1982, *ARA&A*, **20**, 91
- Myers, P. C., Hatchfield, H. P., & Battersby, C. 2022, *ApJ*, **929**, 34
- Padovani, M., Barnes, A. T., Immer, K., et al. 2024, *A&A*, **691**, A70
- Oka, T., Geballe, T. R., Goto, M., Usuda, T., & McCall, B. J. 2005, *ApJ*, **632**, 882
- Oka, T., Geballe, T. R., Goto, M., et al. 2019, *ApJ*, **883**, 54
- Ossenkopf-Okada, V., Csengeri, T., Schneider, N., Federrath, C., & Klessen, R. S. 2016, *A&A*, **590**, A104
- Ostriker, E. C., Stone, J. M., & Gammie, C. F. 2001, *ApJ*, **546**, 980
- Padoan, P., & Nordlund, Å. 2011, *ApJ*, **730**, 40
- Padovani, M., Ivlev, A. V., Galli, D., et al. 2020, *SSRv*, **216**, 29
- Pillai, T., Kauffmann, J., Tan, J. C., et al. 2015, *ApJ*, **799**, 74
- Querejeta, M., Schinnerer, E., Schrubba, A., et al. 2019, *A&A*, **625**, A19
- Rathborne, J. M., Longmore, S. N., Jackson, J. M., et al. 2014, *ApJL*, **795**, L25
- Reid, M. J., Menten, K. M., Brunthaler, A., et al. 2019, *ApJ*, **885**, 131
- Rosolowsky, E., Hughes, A., Leroy, A. K., et al. 2021, *MNRAS*, **502**, 1218
- Rosolowsky, E. W., Pineda, J. E., Kauffmann, J., & Goodman, A. A. 2008, *ApJ*, **679**, 1338
- Russeil, D., Schneider, N., Anderson, L. D., et al. 2013, *A&A*, **554**, A42
- Salaris, M., & Cassisi, S. 2005, Evolution of Stars and Stellar Populations (Chichester: Wiley)
- Schmiedecke, A., Schilke, P., Möller, T., et al. 2016, *A&A*, **588**, A143
- Schneider, N., André, P., Könyves, V., et al. 2013, *ApJL*, **766**, L17
- Schneider, N., Bontemps, S., Girichidis, P., et al. 2015, *MNRAS*, **453**, L41

- Schneider, N., Bontemps, S., Motte, F., et al. 2016, *A&A*, 587, A74
- Schneider, N., Ossenkopf-Okada, V., Clarke, S., et al. 2022, *A&A*, 666, A165
- Schwörer, A., Sánchez-Monge, Á., Schilke, P., et al. 2019, *A&A*, 628, A6
- Shetty, R., Beaumont, C. N., Burton, M. G., Kelly, B. C., & Klessen, R. S. 2012, *MNRAS*, 425, 720
- Sormani, M. C., & Barnes, A. T. 2019, *MNRAS*, 484, 1213
- Sormani, M. C., Sobacchi, E., Fragkoudi, F., et al. 2018, *MNRAS*, 481, 2
- Sormani, M. C., Tress, R. G., Glover, S. C. O., et al. 2020, *MNRAS*, 497, 5024
- Stutz, A. M., & Kainulainen, J. 2015, *A&A*, 577, L6
- Terrier, R., Clavel, M., Soldi, S., et al. 2018, *A&A*, 612, A102
- Terrier, R., Ponti, G., Bélanger, G., et al. 2010, *ApJ*, 719, 143
- Tress, R. G., Sormani, M. C., Glover, S. C. O., et al. 2020, *MNRAS*, 499, 4455
- Walker, D. L., Battersby, C., Lipman, D., et al. 2025, *ApJ*, 984, 158
- Veltchev, T. V., Girichidis, P., Donkov, S., et al. 2019, *MNRAS*, 489, 788
- Walker, D. L., Longmore, S. N., Bally, J., et al. 2021, *MNRAS*, 503, 77
- Walker, D. L., Longmore, S. N., Bastian, N., et al. 2016, *MNRAS*, 457, 4536
- Walker, D. L., Longmore, S. N., Zhang, Q., et al. 2018, *MNRAS*, 474, 2373
- Yusef-Zadeh, F., Hewitt, J. W., Arendt, R. G., et al. 2009, *ApJ*, 702, 178